The Modeling and Characterization of a Lorentz-Force Actuator for Needle-Free Injection

by

Jonathan Michael Mendoza

Submitted to the Department of Mechanical Engineering
in partial fulfillment of the requirements for the degree of

Bachelor of Science in Mechanical Engineering

at the

MASSACHUSETTS INSTITUTE OF TECHNOLOGY

June 2011

Author .....
Department of Mechanical Engineering
May 11, 2011

Certified by .....
Ian Hunter
Hatsopoulos Professor of Mechanical Engineering
Thesis Supervisor

Accepted by .....
John H. Lienhard V
Collins Professor of Mechanical Engineering
Chairman, Undergraduate Thesis Committee

The Modeling and Characterization of a Lorentz-Force Actuator for Needle-Free Injection

by

Jonathan Michael Mendoza

Submitted to the Department of Mechanical Engineering
on May 16, 2011, in partial fulfillment of the
requirements for the degree of
Bachelor of Science in Mechanical Engineering

Abstract

The BioInstrumentation Laboratory at MIT developed a needle-free injector that is driven by a Lorentz-force actuator. The current model was able to generate pressures of up to 20 MPa in order to drive a jet of water based solution. In order to improve the needle-free injector, a new Lorentz-force actuator was designed and modeled using finite element analysis software. The new magnetic configuration included a radially-magnetized ring that generated a larger magnetic field across the airgap of the Lorentz-force actuator. Calculated peak forces were between 400 N and 600 N depending upon the position of the stroke length and the current density through the coil. Saturation in the steel core and casing, onsetting at a current density of about 10^8 A/m^2, resulted in diminishing returns in force from an increasing current density. The rheological properties of poly(ortho) ester were measured for determining the feasibility of injecting viscous drug mediums. Of the two samples provided, the less viscous batch had a measured viscosity of 2.5 Pa·s and exhibited shear thinning at a shear rate of about 1000 s^{-1}. Shear thinning has a large effect on the required pressure for injecting poly(ortho) ester at sufficient velocities. Finally, a benchtop experiment was designed and built to measure the force output of a BEI Kimco Lorentz-force linear actuator. A circuit was built to charge and discharge a capacitor that drives the output of the coil. Forces of up to 1000 N were measured at a stored capacitor voltage of 200 V. The time to peak force output was measured between 4 and 5 ms for high and low voltages respectively. Inefficient switching resulted in lower than expected forces below 40 V while increased resistance increased the damping of the overall system. Saturation was observed in the coil at voltages of 70 V and higher. The current capacity of the coil will continue to be pushed to the maximum stored value of 500 V.

Thesis Supervisor: Ian Hunter
Title: Hatsopoulos Professor of Mechanical Engineering

Acknowledgments

I would like to thank Professor Ian Hunter for providing me with the opportunity to work in his lab and utilize the resources available to his students. I would like to acknowledge the students of the BioInstrumentation Laboratory for having the patience to deal with my tendancies to ask questions before moving forward with my research. I would like to thank my mother, Annette Mendoza, for always emphasizing the importance of intellectual pursuit throughout my childhood years. I would not be where I am today without her love, support, and advice. I would like to thank my father, William Mendoza, for his unwavering dedication to his children and for the practical mechanical skills he taught me over the years. His knack for practical building was a large influence on my decision to become a mechanical engineer. I would like to thank my brother, Christopher Mendoza, for being the best role model I could ever ask for. Despite our age difference, he was always willing to spend time and make sacrifices for me (sorry about the car). I would like to thank Katie Treuer for her constant encouragement throughout this process. Finally, I would like to thank Dodd Gray for his presence and advice during the weary hours past midnight.

Contents

List of Figures

Chapter 1

Introduction

The most widely used method of parenteral drug delivery is accomplished through the use of a needle and a syringe. Although practical, complications from this route of drug administration, such as infection, pain, and trypanophobia, have served as a motivation for the development of a new method to deliver drugs through the skin. Over the past decade, needle-free injection has been accomplished through the pressurization of a drug in liquid or powder form. Although the pressure required is dependent upon various factors such as the viscosity of the drug, the geometry of the nozzle, and the desired depth of injection [1], needle-free injectors have been successful in driving jets of drugs through the skin. Various methods have been developed in order to generate pressures quickly enough for the purposes of needle-free injection. Although systems utilizing nonlinear springs and compressed air have been able to sufficiently pressurize the drug, these methods do not have adequate control over the timescale of the injection [2]. A piezoelectric actuated system developed at UC Berkeley has provided one method in the improvement of the controllability of the jet injection. Unfortunately, the volume of injection is limited to about 1 μL [3].

1.1 Lorentz Force Actuation

The BioInstrumentation Lab at MIT has provided an alternative approach to this challenge. By storing and releasing electrical energy, pressurization is achieved through

electromechanical actuation. Voltage, pressure, and position are monitored and allow for controllability and repeatability in the velocity profile of the jet over the timescale of the delivery. A Lorentz-force linear actuator is an electromechnical motor that generates high forces due to a current in the presence of a magnetic field. Although Lorentz-force actuators were not practical for handheld usage due to their large size requirements, the advent of rare-earth magnets, Neodynium-Iron-Boron specifically, has allowed for drastic size reduction due to their high coercivity, magnetic energy density, and resistance to demagnetization [2].

1.2 Capabilities and Limitations

The portable version of the needle-free injector developed by the BioInstrumentation Lab is capable of providing pressures of up to 20 MPa. While the device is able to inject up to 250 μL, the velocity profile control has been optimized around an operating point for 50 μL deliveries. Using the pressure profile for this desired volume delivery, the volume of fluid delivered per shot was $50.9 \pm 1\mu$L [1]. At a pressure of 20 MPa, the needle-free injector is able to drive water based solutions at a velocity of 200 m/s. While these velocities are achievable at viscosities on the order of magnitude of 10^{-3} Pa·s, the pressure required to achieve this jet velocity will increase as a function of viscosity.

While water-based solutions are practical for the operating range of the current needle-free injector, there are better mediums for the purpose of drug delivery. The BioInstrumentation Lab is in the process of investigating the ability to inject polymeric liquids. Poly(ortho) ester, more specifically POE IV, has shown promising attributes that allow for a synthesis which provides controllability in its mechanical and thermal properties, erosion rates, and drug release rates [4]. Although poly(ortho) esters can be synthesized to have a wide range of rheological properties, from solid to gel-like, the viscosity of the polymeric liquid is on the order of magnitude of 1 Pa·s or greater. Jet injection of fluids with viscosities this high is unfortunately not possible with the current devices.

Due to the ever increasing nature of computation power and efficiency in computational algorithms, finite element analysis modeling software is able to provide insight into the electromagnetic fields that govern the behavior of Lorentz-force actuators. With the use of such powerful tools, better designs can be made to increase the force output of a Lorentz-force actuator with a given magnetic field. This thesis discusses the electromagnetic modeling of a new Lorentz-force actuator design as well the design and results of an experiment that characterizes a premade Lorentz-force actuator that could potentially generate enough pressure to drive poly(ortho) ester at velocities sufficient for injection.

Chapter 2

Current NFI Design

The needle-free injector developed by the BioInstrumentation Laboratory comes in both a handheld and laboratory benchtop model. Both models consist of an injector, a power supply, and a real-time controller. The benchtop device is driven by a 4 kW linear power amplifier while the handheld device is powered by a low inductance electrolytic capacitor. The real-time controller connects to a computer in order to make quick adjustments to the profile of the injection. If interactive control or a computer is not required, the hand held device can operate utilizing its preset current control scheme [5].

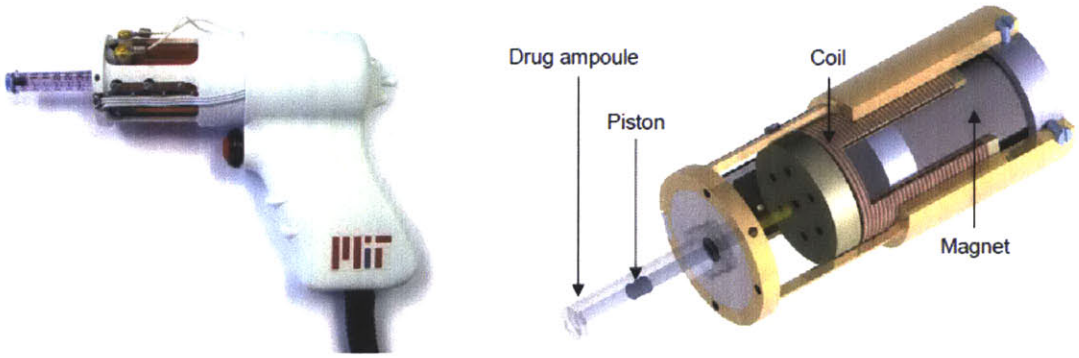

Figure 2-1: Handheld needle-free injector (left) and Lorentz-force actuator (right) taken from [5].

2.1 The Injector

The core of the Lorentz-force actuator comprises of two 0.4 MN/m^2 Neodynium-Iron-Boron magnets inside a 1026 carbon-steel casing. The magnetic flux density generated by the magnets is approximately 0.6 T in the radial direction with the proper airgap spacing and iron to complete the field loop. The coil of the Lorentz-force actuator consists of 582 turns of 360 μm diameter enameled copper wire. It is important to reduce the mass and damping as much as possible in the moving coil. Weight reduction was accomplished by machining the voice coil former out of Acetal copolymer. The total mass of the moving assembly is about 50 g [1]. Damping in a Lorentz-force actuator stems from the eddy currents generated by a moving conductor through a magnetic field; consequently, these effects are mitigated due to the fact that Acetal copolymer is not conductive.

2.1.1 Electromechanical Model

The DC resistance of the Lorentz-force actuator was measured to be 11.3 Ω while the inductance was measured to be 4.6 mH [1]. In the most simplistic form, this system can be modeled as one that takes an input of voltage from a controller and outputs a velocity of the jet.

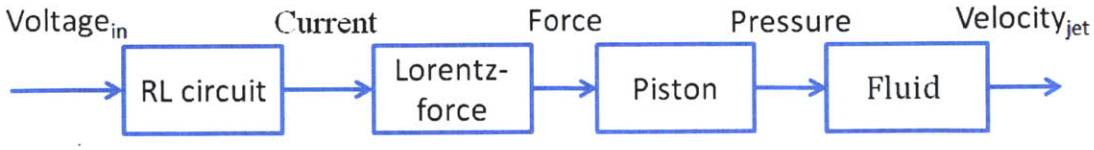

Figure 2-2: Block diagram of open loop system.

In order to have an idea of how the inputs of each subsystem are transduced into their respective outputs, it is important to consider the time constants of each subsystem and weigh their significance upon the system as a whole. It seems practical to begin with the relationship between voltage (V) and current (I). Kirchoffs law

defines this relationship as,

$$V = IR. \tag{2.1}$$

The resistance is then defined as the sum of the impedance of the system in the Laplace domain. The transfer function of the RL circuit is then,

$$\frac{I}{V}(s) = \frac{1}{Ls + R}. \tag{2.2}$$

First-order systems can be put into the form,

$$\frac{Y}{X}(s) = \frac{K}{\tau s + 1}, \tag{2.3}$$

where Y is defined as the output, X is defined as the input, K is an arbitrary gain, and τ is the time constant of the system. In the time domain, the response to a unit step function is then,

$$y(t) = (1 - e^{-\frac{t}{\tau}})K. \tag{2.4}$$

Clearly, the time constant of the RL circuit of the actuator is then,

$$\tau = \frac{L}{R} = 4.1 \cdot 10^{-4}\ s. \tag{2.5}$$

Since the time scale of the peak velocity of the jet is on the same order of magnitude as the rise time of the current, the transient effects of this first order system cannot be ignored.

The force generated from a current in a magnetic field can be described by the Lorentz force. The force on a point charge due to an electromagnetic field is,

$$\mathbf{F} = q[\mathbf{E} + (\mathbf{v} \times \mathbf{B})], \tag{2.6}$$

where $\mathbf{F}$ is the force (N), $\mathbf{E}$ is the electric field (V/m), $\mathbf{B}$ is the magnetic field (T), q is the electric charge (C), and $\mathbf{v}$ is the velocity of the charged particle (m/s). The

force on a current carrying wire is then,

$$\mathbf{F} = I\mathbf{L} \times \mathbf{B}, \tag{2.7}$$

where $\mathbf{L}$ is a vector whose magnitude is the length of the wire (m) and direction is the direction along the wire. The relationship between current and force for this Lorentz-force is defined as force sensitivity and has a value of 10.8 $\pm$ 0.5 N/A at mid-stroke.

The transfer function that describes the transduction of the force from the coil to the force in the piston can also be described as a first order system with a time constant that is inversely proportional to the stiffness of the piston. If the time constant is in seconds and the stiffness is in N/m, then the time constant is proportional to a term that has the units of kg/s, which is an inertia corresponding to the deformation of the piston.

The relationship between force and the development of pressure in the ampoule can also be approximated as a first-order system. Pressure travels at the speed of sound in the medium, therefore the time constant is the time it takes for the pressure to travel across the entire length of the ampoule (25 mm). The speed of sound in water at room temperature is 1497 m/s, thus the time constant of the system is calculated to be $2.2 \cdot 10^{-5}$ s. Because this time constant is orders of magnitude below the time scale of the injection time, it is reasonable to assume that the force of the piston and the pressure inside the fluid do not have transient dependence. The physics of the ampoule and piston, however, does have a time dependence.

The ampoules chosen for the injector were manufactured by Injex (part #100100). These ampoules are cost-effective and reliable, especially considering the fact that they are designed for use in a commercially-available jet injector system (Injex 30). The cross sectional area of the bore of the piston is approximately 10^{-5} m^2 and has a length of 30 mm which corresponds to an available volume of 300 μL. The internal diameter of the ampoule tapers at the tip to an orifice with a diameter of 220 $\pm$ 5 μm. The ampoules have a lifetime of about 50 to 100 injections [5].

The effects of viscosity are considered in the estimation of the flow out of the orifice of the ampoule. The Reynolds number is a dimensionless value describing the ratio of inertial forces to viscous forces. To drive water, which has a density of approximately $\rho = 1000$ kg/m^3 and a viscosity of approximately $\mu = 10^{-3} Pa \cdot s$ at a velocity of $V = 200$ m/s through an orifice of diameter $D = 220\ \mu m$, the Reynolds number can be calculated as,

$$Re = \frac{\rho V D}{\mu} = 44000. \tag{2.8}$$

Inertial forces clearly dominate this flow; consequently, the effects of viscosity can be ignored. Incompressible and inviscid flow can then be used to approximate the flow through the nozzle orifice. Bernoulli's principle, which is derived from the conservation of energy, states that,

$$\frac{v^2}{2} + gz + \frac{p}{\rho} = constant, \tag{2.9}$$

where p is pressure (Pa), g is the gravitational constant, and z is the height (m). This equation is valid at any point along a streamline. Therefore the outlet velocity can be approximated as,

$$v = \sqrt{\frac{2p}{\rho}}. \tag{2.10}$$

Because the actual velocity of the jet is hard to measure for the purpose of real-time control, a linear slide potentiometer is used to measure the position of the coil. By knowing the position of the piston, the derivative of the position over time can be used to approximate the velocity of the jet since,

$$v_{jet} = \frac{A_{amp}}{A_{noz}} v_{coil}, \tag{2.11}$$

where A_{amp} is the cross sectional area of the inner diameter of the ampoule while A_{noz} is the cross sectional area of the nozzle orifice.

2.2 The Controller

Servo control of the needle-free injector is accomplished through the use of a compact reconfigurable input-output system (cRIO). The compact RIO utilizes a field-programmable gate array (cRIO-9104) that interfaces with a real-time controller (cRIO-9004). The real-time controller runs a LabView program on a 200 MHz Pentium microprocessor that is responsible for setting the trajectory, user commands, and feedback control.

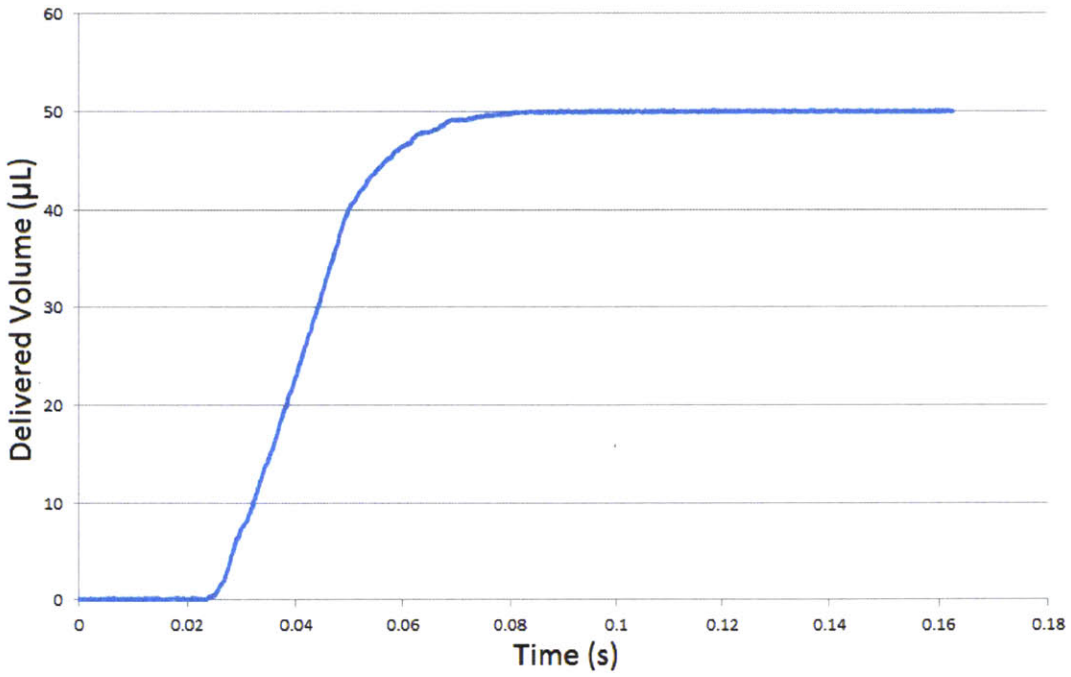

Figure 2-3: Example waveform of delivered volume during injection.

The FPGA runs the closed loop control of the coil position at a rate of 64 kHz. The analog output from the compact RIO chassis is amplified by a linear power amplifier (LVC5050). The amplified analog output drives the Lorentz force actuator up to a maximum power output of 4 kW. The voltage and current of the linear power amplifier are monitored by the compact RIO. The digitized version of these analog waveforms are stored and sent to a computer for post-processing and analysis.

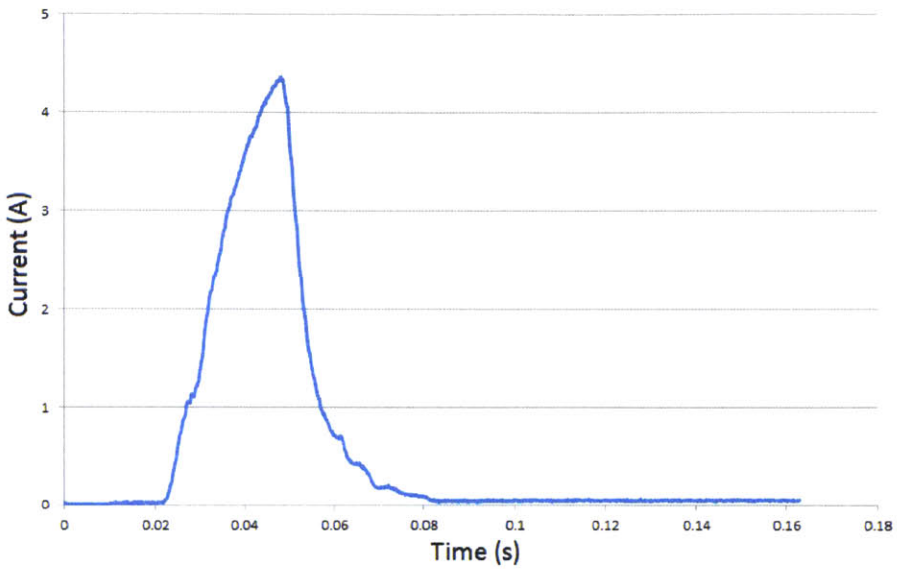

Figure 2-4: Example waveform of current during injection.

Strain gages connected to the ampoule are used to measure the pressure of the injection. These analog waveforms are also digitized and stored by the compact RIO.

The graphical user interface in LabView allows for customization of the desired velocity profile of the injection [5]. The velocity profile can be separated into two phases. The duration and magnitude of the initial high velocity pulse determines the depth of the injection. The duration of the high velocity jet is usually on the order of 10 ms. The second regime is a constant low velocity profile that governs the total volume delivered by the needle-free injector [6].

The GUI provides the user control over the velocity of the jet (v_{jet}), the time duration of the high velocity jet (T_{jet}), the constant low velocity magnitude (v_{follow}), and the total injection volume (V). The velocity profile determined by the user input is then generated by a 1 kHz spline interpolator. The position of the Lorentz-force actuator is also able to be controlled in manual mode for the purposes of the expulsion of air or to draw fluid into the ampoule [5].

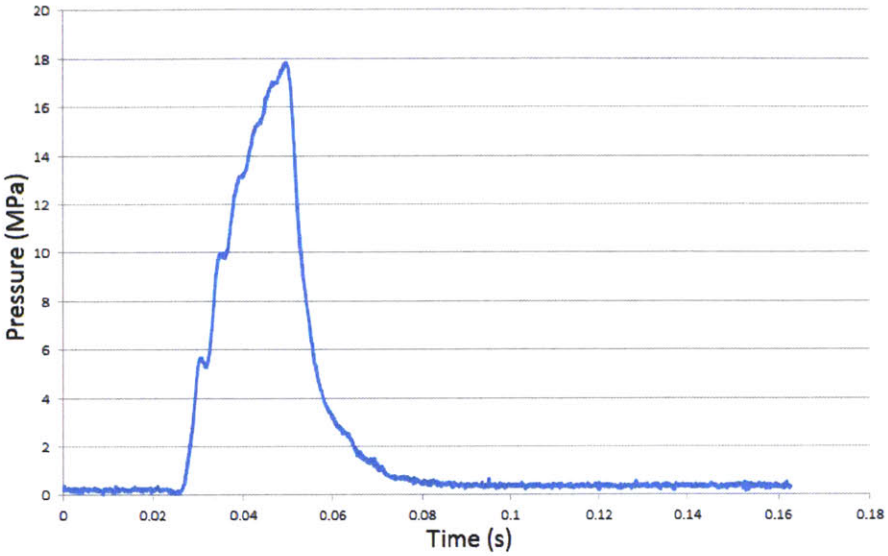

Figure 2-5: Example waveform of pressure during injection.

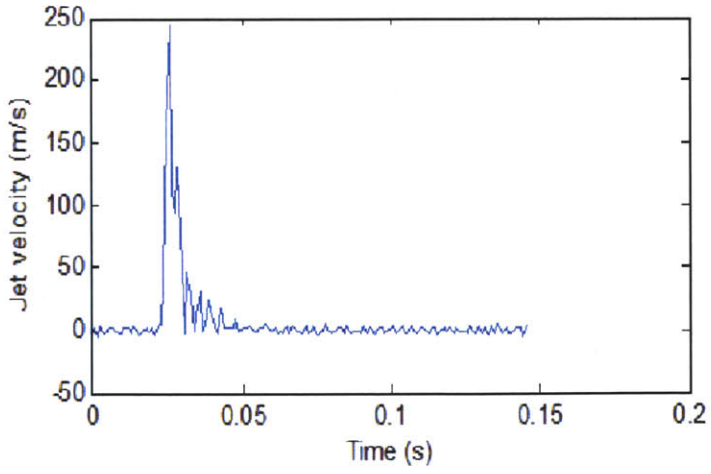

Figure 2-6: Example waveform of velocity during injection.

Chapter 3

Modeling the Lorentz-Force Actuator

ANSYS [7], a finite-element analysis software package, is used to model the current magnetic configuration of the needle-free injector in order to optimize the performance of the Lorentz-force actuator.

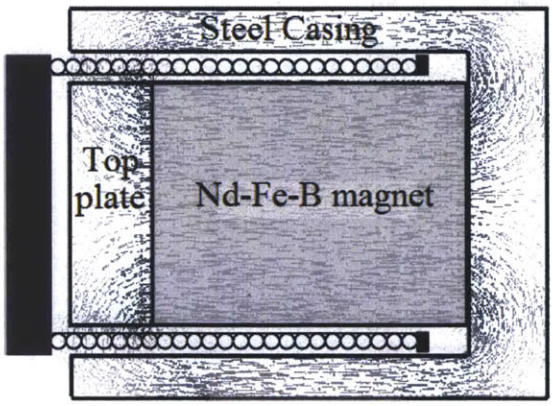

Figure 3-1: Magnetic configuration of current Lorentz-force actuator taken from [2].

The overall diameter of the Lorentz-force actuator is 43 mm and the overall height is 48 mm. The diameter of the core of Lorentz-force actuator that includes the two Neodynium-Iron-Boron magnets and the steel top plate is 25 mm. The width of

the air gap is 3 mm while the cross-sectional thickness of the coil is 2.5 mm. The height of the coil is 32 mm. The thicknesses of the top and bottom plate are 6 mm. The thickness of the outer steel wall is 6 mm. The given dimensions and material properties of the steel, Neodynium-Iron-Boron, and copper, are modeled in ANSYS. The time-independent solution provides insight into the behavior of the magnetic field within the Lorentz-force actuator. Maxwell's equations of electromagnetism are solved in two-dimensional, axisymmetric mode using cylindrical coordinates.

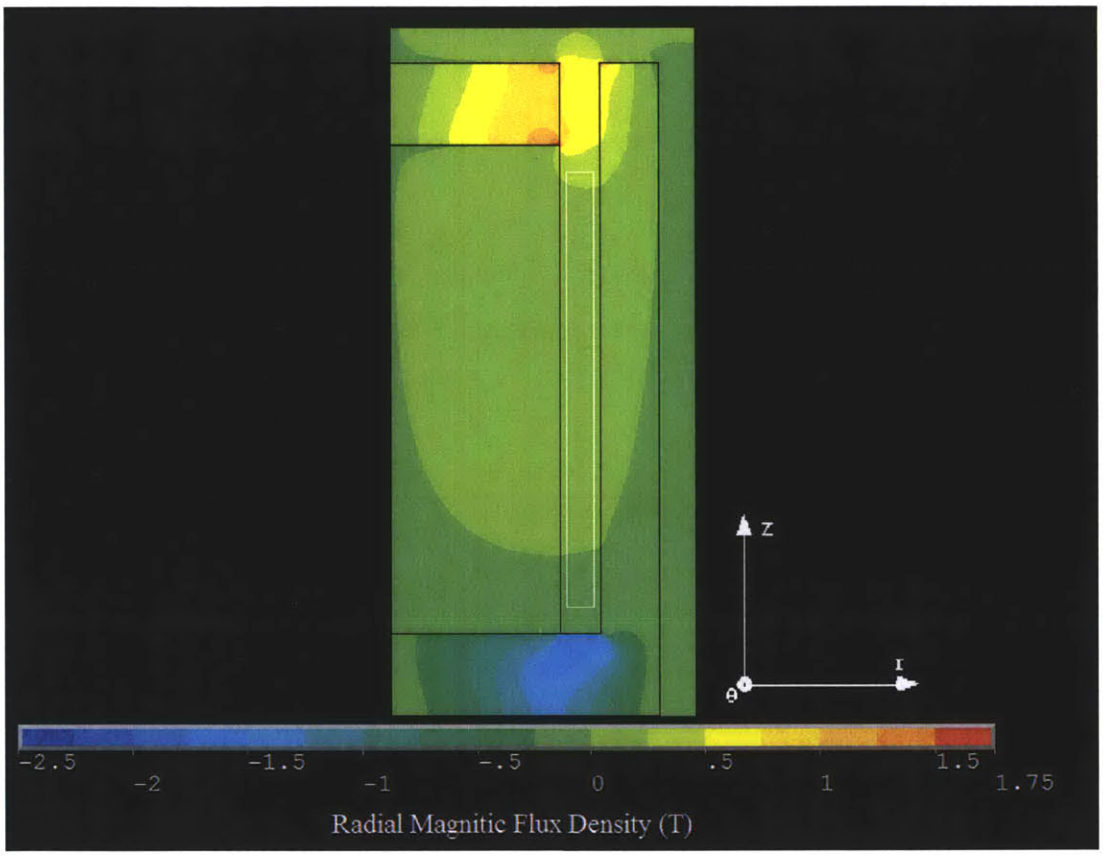

Figure 3-2: Radial magnetic flux density of the current Lorentz-force actuator.

As previously predicted, the magnetic flux density in the radial direction was calculated to be about 0.6 T. As seen in the solution, only a small portion of the coil is exposed to the magnetic field. In order to utilize the full capacity of the force output of the coil, it is important to have a magnetic field that is strong in the

radial direction across the entire length of the coil. The magnetic flux lines yield a visualization of the magnetic circuit within the Lorentz-force actuator.

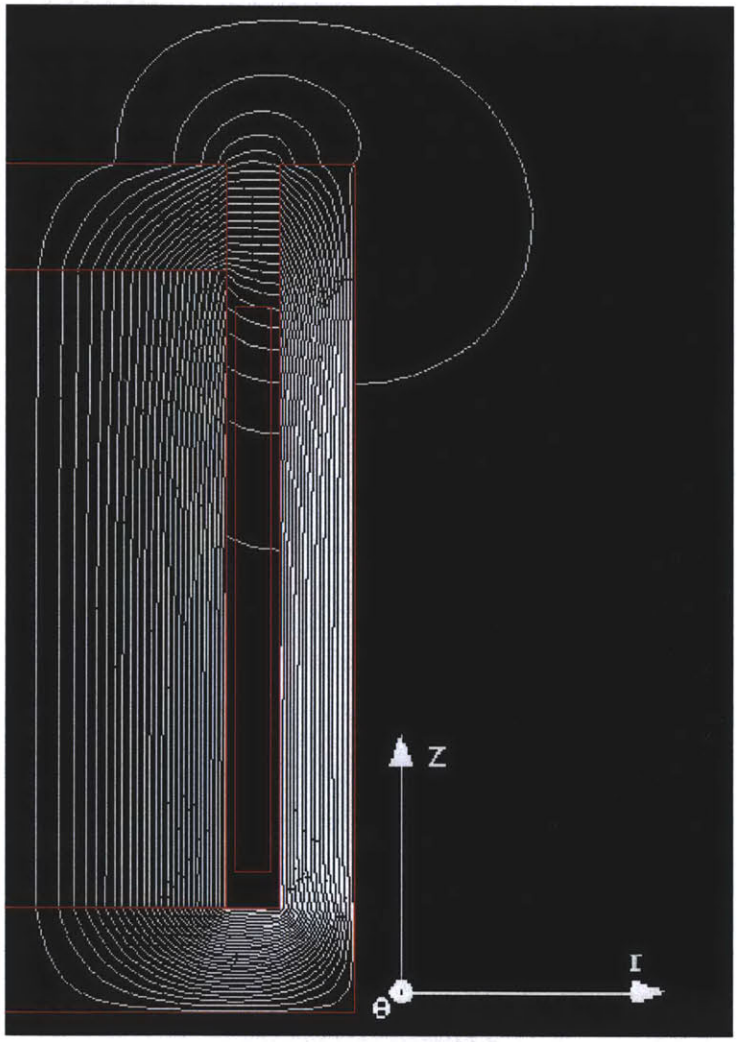

Figure 3-3: Magnetic flux lines of the current Lorentz-force actuator.

The drawbacks of a unidirectional magnetic circuit stem from the relationship between magnetic flux intensity (**B**) and auxiliary magnetic field (**H**). The linear approximation is described as,

$$\mathbf{B} = \mu \mathbf{H}, \tag{3.1}$$

where the scalar μ is the permeability. Permeability is the measure of the ability of a material to support a magnetic field (**B**). The purpose of using M3 steel, which is ferrous, is due to its high value of permeability. It will be more suited to maintaining a high magnetic flux density than a non-ferrous material; consequently, there will be a larger magnetic field across the air gap to generate greater force in the voice-coil. Although permeability is treated as a material property with a constant value in the above equation, the value is dependent upon the magnitude of **H**. As **H**, whose increase in this context arises from the magnets and the current through the coil, gets larger, the value of permeability in steel will asymptotically approach that of paramagnetic materials which is three orders of magnitude lower. This reduction in permeability is known as saturation. As saturation occurs within the casing of a Lorentz-force actuator, there will be significant diminishing returns in the force output per unit of current flowing through the coil. In other words, there will no longer be a linear relationship between current and force output. The concept of saturation is crucial to highlighting the drawbacks of a unidirectional magnetic circuit. The direction of the flux lines in the magnetic circuit in the figure above is clockwise. If the current in the coil is flows into the page, the auxiliary magnetic field is in the same direction as the magnetic circuit. The onset of saturation will occur at lower currents for the given configuration in comparison to the other direction. The unidirectional magnetic circuit distorts the symmetry of the force output for a given direction of current.

3.1 The New Lorentz-Force Actuator

A delivery volume of 250 μL of fluid with a piston that has a cross sectional area of 10^{-5} m^2 requires a stroke length of at least 25 mm. The new Lorentz-force actuator design will have a stroke length of 30 mm which fulfills the volume delivery requirement. In order to have similar force outputs for the same magnitude of current in opposing directions, the magnetic circuits needs to be symmetric about the axis tangential to the field across the air gap. BEI Kimco Lorentz-force linear actuators

(LA series) utilize a design that incorporates a magnetic core that consists of two magnets whose dipoles point in the opposite directions. This configuration results in two magnetic circuits that travel in opposite directions but have the same direction across the air gap. By incorporating this magnetic configuration with two oppositely wound coils, the bi-directionality of the force output is significantly improved. Although this design reduces the direction dependence of current upon force output, the size of the magnetic field is not large enough to span the entire length of the copper coil.

New techniques in magnetic materials manufacturing allow for the magnetization of a ring with its magnetic moment pointing radially outward or inward. If this radially magnetized ring is placed within a symmetric steel casing, the magnetic circuits will be similar to the configuration of the BEI Kimco design. Additionally, a magnetic field of a larger size in the radial direction will be generated across the air gap. For the finite-element modeling of the new Lorentz-force actuator design, the materials selected are M3 steel for the casing, copper for the coil, and Neodynium-Iron-Boron for the radially magnetized ring.

The solution to the system's magnetic field without the presence of current in the coil provides a good estimate of the magnitude and behavior of the magnetic field within the new Lorentz-force actuator design. The slight lack of symmetry in the magnetic field across the air gap is due to the opening in the top of the actuator. The lack of a smooth gradient in the steel core is due to the the onset of saturation in the steel. It is much easier for ANSYS to solve for unsaturated materials or fully saturated ones. If the solution happens to fall in the transition region, discontinuities will be present in the final solution. The magnitude of the magnetic flux density in the radial direction across the copper coil is about 0.75 T. Although this is not much larger than the field generated by the original Lorentz-force actuator design, the magnetic field crosses the entire length of the coil, resulting in higher force output. The magnetic circuits in this configuration are best visualized by the ANSYS solution.

At mid-stroke, the force in the coil should be similar in value for currents in both directions. The magnitude of magnetic flux density at which steel begins to saturate

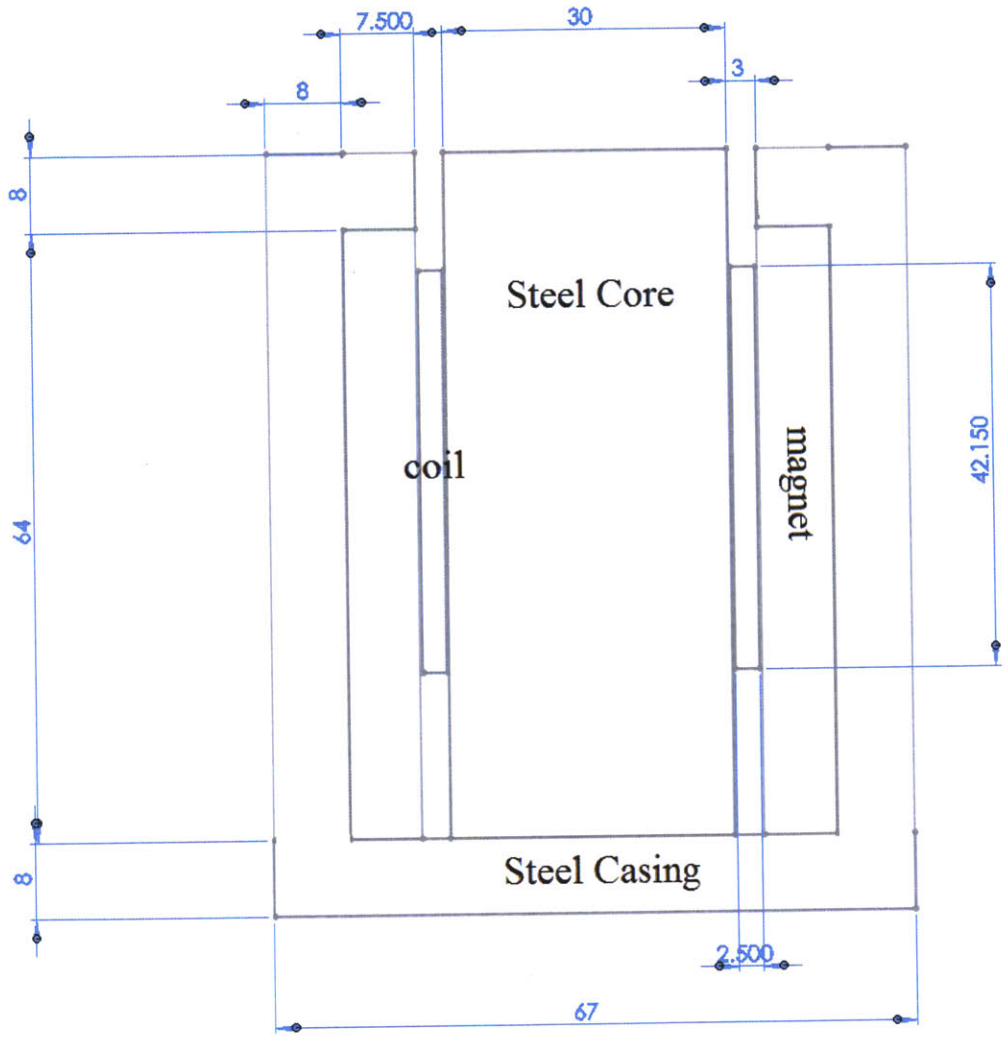

Figure 3-4: Dimensioned Sketch of New Magnetic Configuration (in mm).

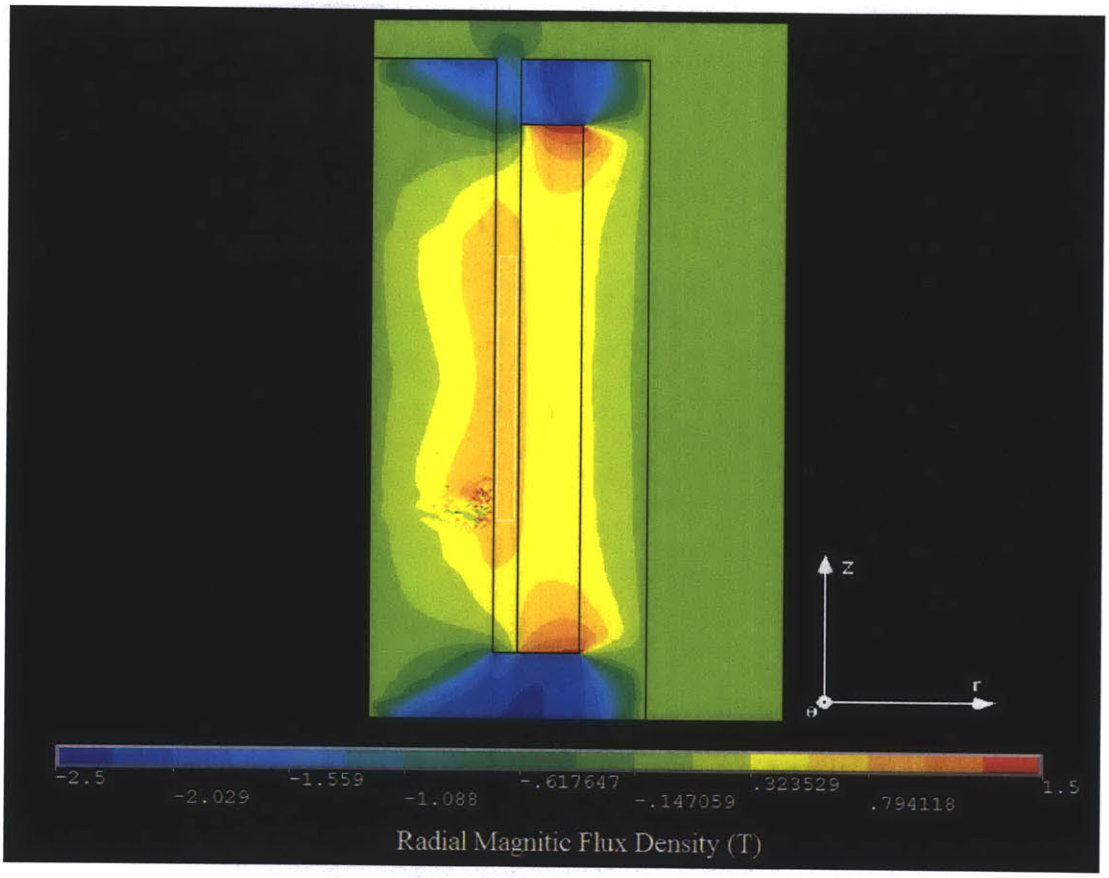

Figure 3-5: Solution of radial magnetic field without current.

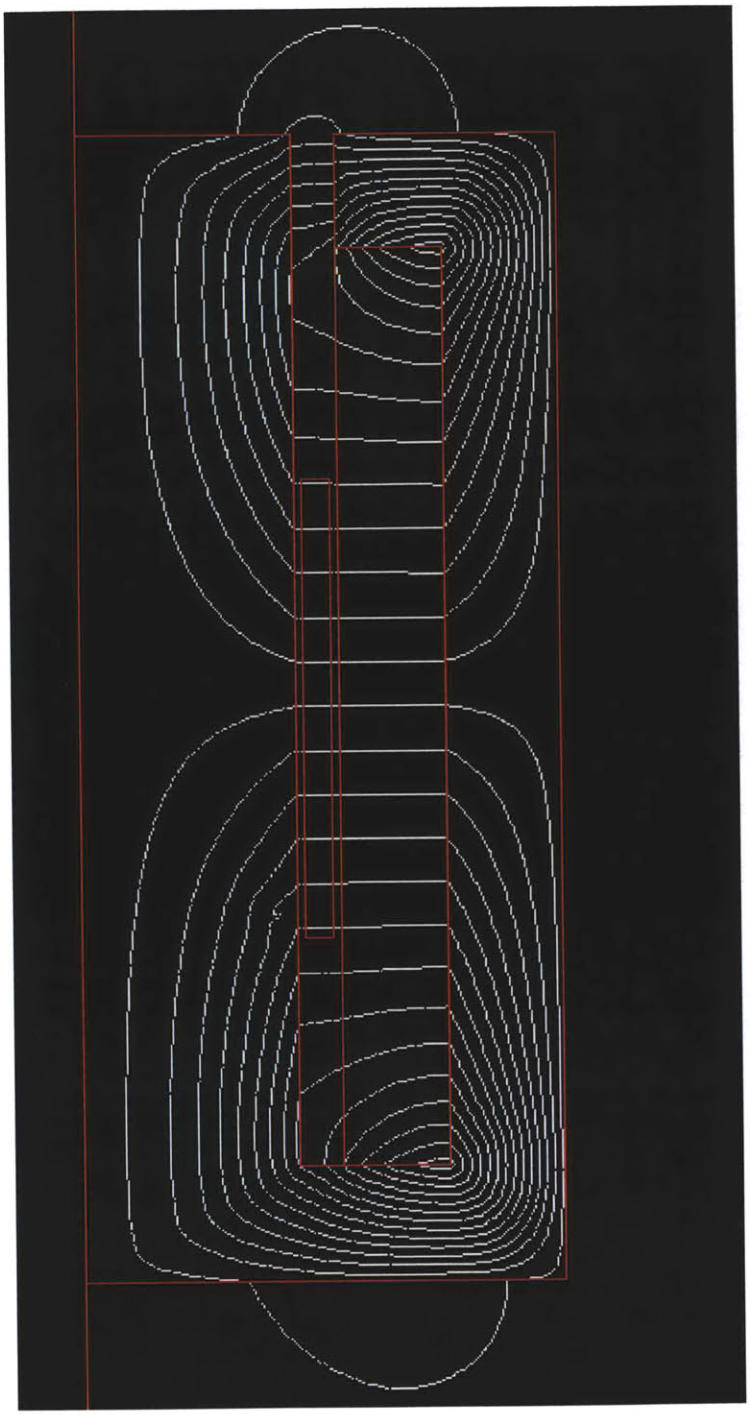

Figure 3-6: Magnetic flux lines without the current.

is between 1.2 and 1.4 T. Saturation in the steel casing can be best represented by the solution showing the absolute magnitude of the magnetic flux density in the Lorentz-force actuator.

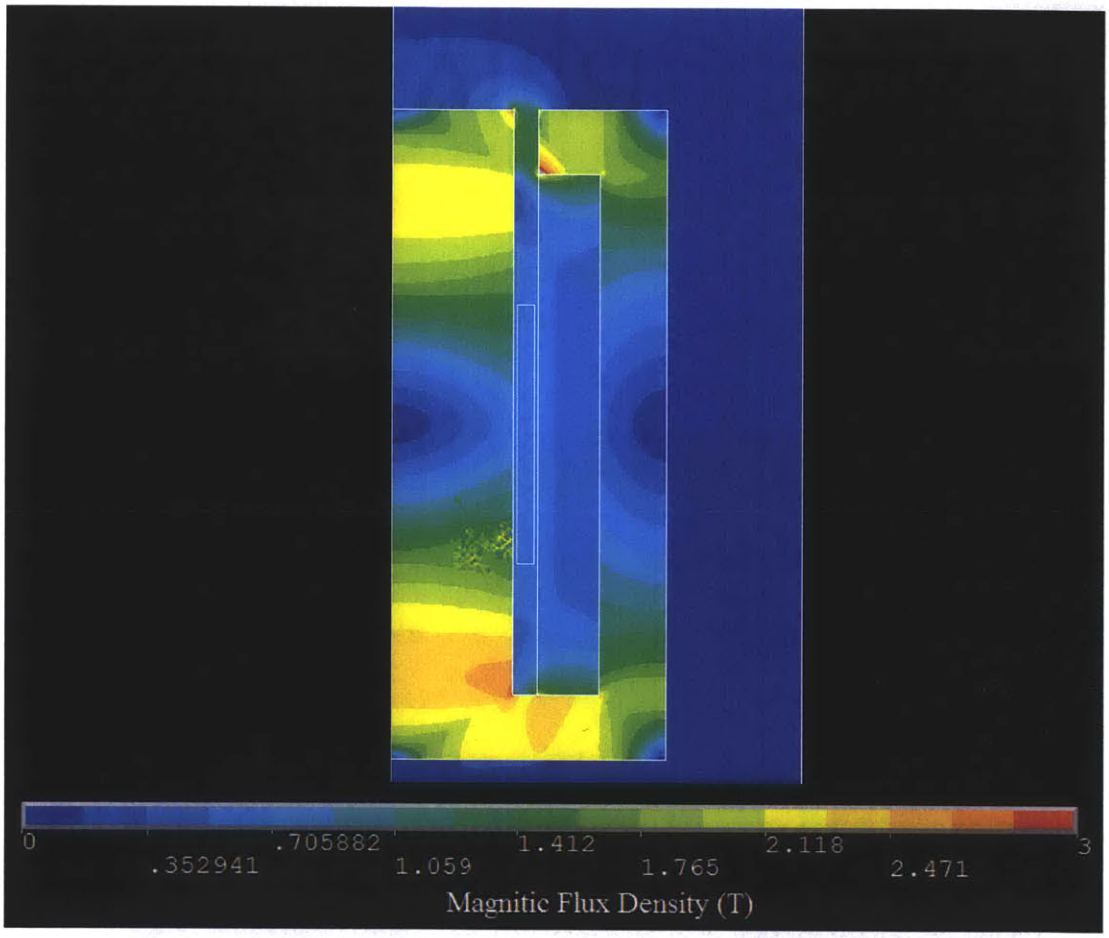

Figure 3-7: Magnitude of magnetic flux density without the current.

In addition to providing clues about the location of saturation in the steel casing, the plot of the absolute magnitude of the magnetic flux density demonstrates the fulfillment of the boundary condition requiring,

$$\mathbf{B} \cdot d\mathbf{A} = 0. \tag{3.2}$$

This boundary condition requires a sufficiently sized air gap to ensure that the solution converges. If the air gap was too small, iterations of the solution would have non-zero magnetic flux density normal to the boundary. When the current is turned off, most of the saturation occurs at the top and bottom of the steel core. The magnitude of the magnetic flux density is lower in the top portion of the steel core due to the flux leakage due to the air gap across the magnetic circuit.

The solution to the magnetic field with the current turned off allows one to understand and compare the effects of the auxiliary magnetic field generated by the current in the coil. Because the current density in the coil will be as large as $3 \cdot 10^8$ A/m^2, the auxiliary magnetic field due to the coil will have a significant effect upon the magnetic flux density across the air gap. Due to the effects of the current, the magnetic flux

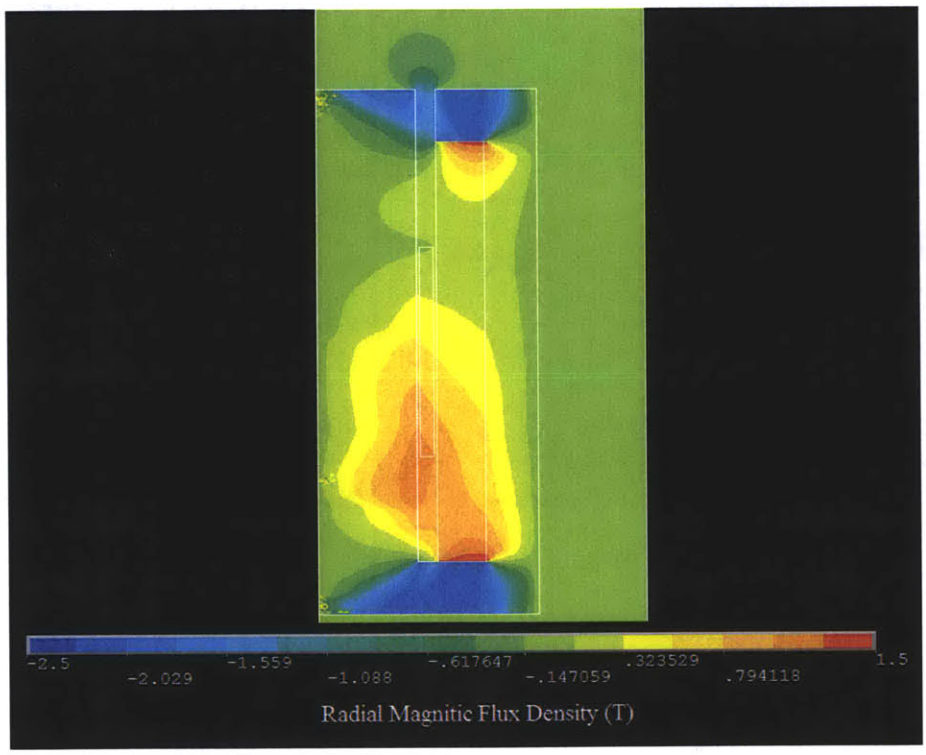

Figure 3-8: Solution of radial magnetic field with a current density of 10^8 A/m^2.

density across the air gap loses its symmetry. There now exists a gradient in the

magnetic field that is highest at the bottom of the coil and lowest at the top of the coil. The magnetic flux lines shed insight into the behavior of the magnetic field in the presence of a large current.

Since the current for this solution is traveling out of the page, the induced magnetic field is oriented downwards inside of the coil and upwards outside of it. As a result, the upper magnetic loop is larger relative to the bottom loop because it is traveling in the same direction as the induced magnetic field from the current in the coil. If current was traveling into the page, the bottom loop would be larger relative to the upper loop for the aforementioned reasons. The reason for the gradient in the radial magnetic flux density across the air gap can be explained by the differences between the flux lines on the inside of the magnetic loop and the ones on the outside. The magnetic flux travels along the path of least resistance; consequently, the upper flux lines travel further down the core of the magnet due to the auxiliary magnetic field. The magnitude of the magnetic flux density of the inner flux lines are primarily in the negative z-direction when they cross the air gap. In other words, the flux lines are analogous to the trajectory of a particle subject to a potential in the radial direction. The magnet in this case is a potential sink on the inner portion of the magnet and a potential source on the outer portion. The outer flux lines travel further along z-direction subject to a potential in the radial direction, thus the magnitude of the magnetic flux density is higher at the bottom of the coil. This argument can also be applied to the gradient of the magnetic field from the bottom of the coil to the bottom of the air gap.

One major consequence of this magnetic configuration is the presence of a magnetic flux in the negative radial direction in the air gap above the radially magnetized ring. In order to allow for a stroke length of 30 mm, the design has to be dimensioned to make sure that the coil does not travel into the region of negative radial magnetic flux. By increasing the aspect ratio to account for this trade off, the size of the magnetic field in the radial direction is increased at the cost of its magnitude. The given dimensions were chosen to allow for a significant force output across the entire stroke of the coil. The force outputs were calculated at mid-stroke, with -15

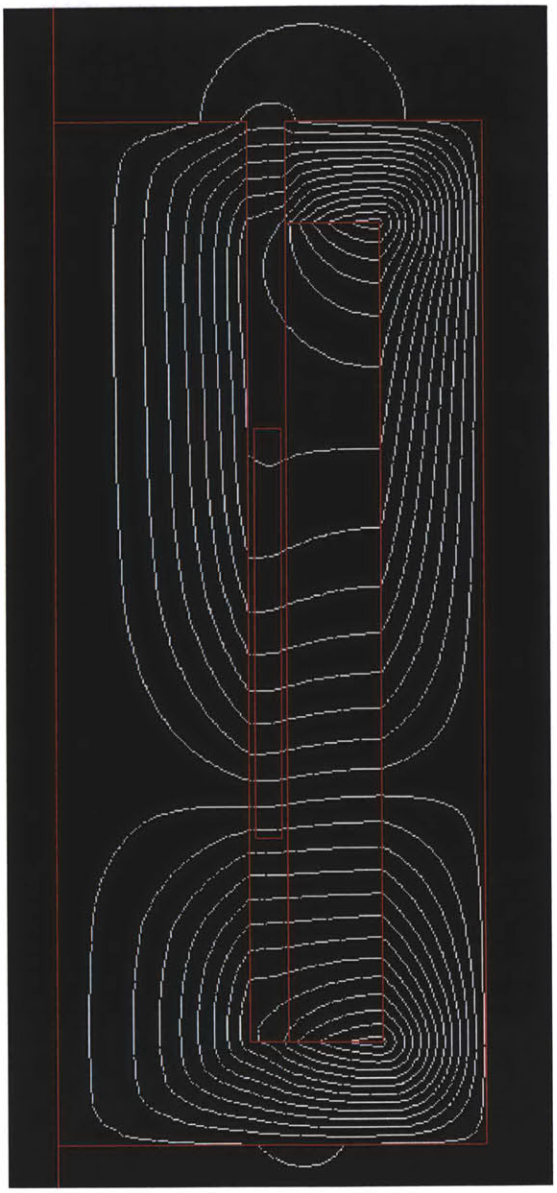

Figure 3-9: Magnetic flux lines with a current density of 10^8 A/m^2.

mm offset, and +15 mm offset for current density values between 0 and $3 \cdot 10^8$ A/m^2 in both directions.

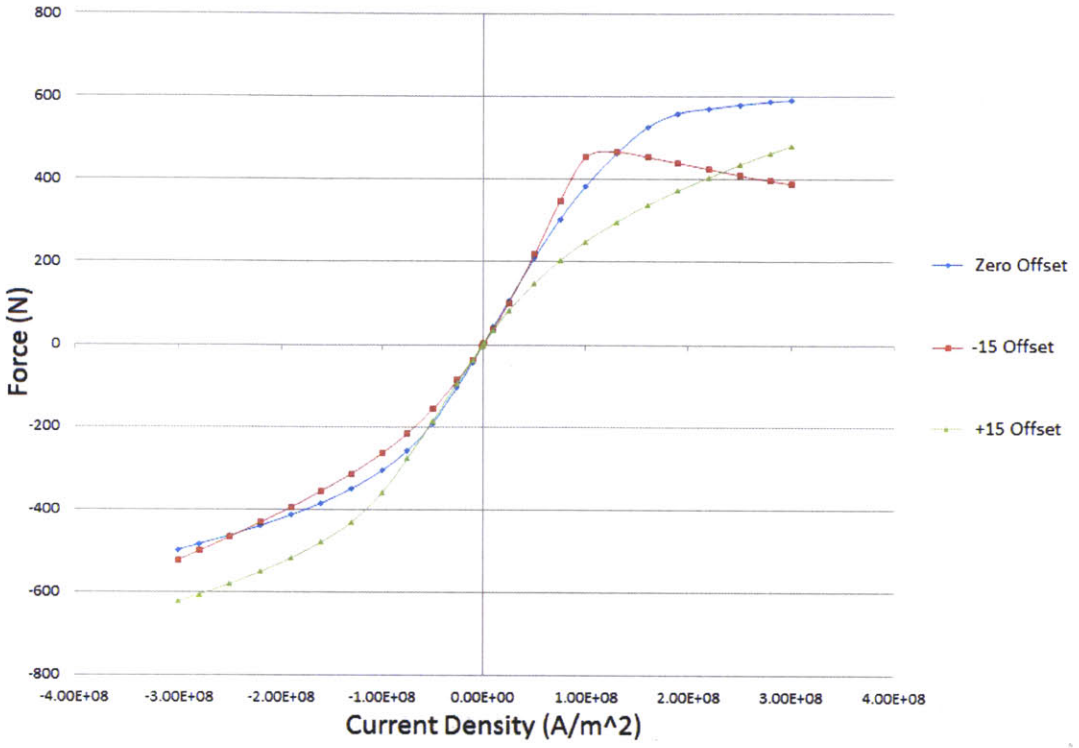

Figure 3-10: Force outputs at the bottom, mid, and top stroke for different current densities.

The deviation from the linear relationship between current and force at a current density of $5 \cdot 10^7$ A/m^2 is the consequence of saturation stemming from the induced auxiliary magnetic field from the coil. The most interesting result of these calculations is the decrease in force output at the -15 mm offset for current densities above $1.3 \cdot 10^8$ A/m^2.

By looking at the most extreme example of this behavior when the current density is at its maximum value of $3 \cdot 10^8$ A/m^2, the induced auxiliary field from the current is so large that the upper magnetic loop dominates to the extent to which it is essentially one loop. This ultimately results in a reduction in the magnetic field that crosses the coil and an increase in the magnetic flux in the negative direction across the air gap

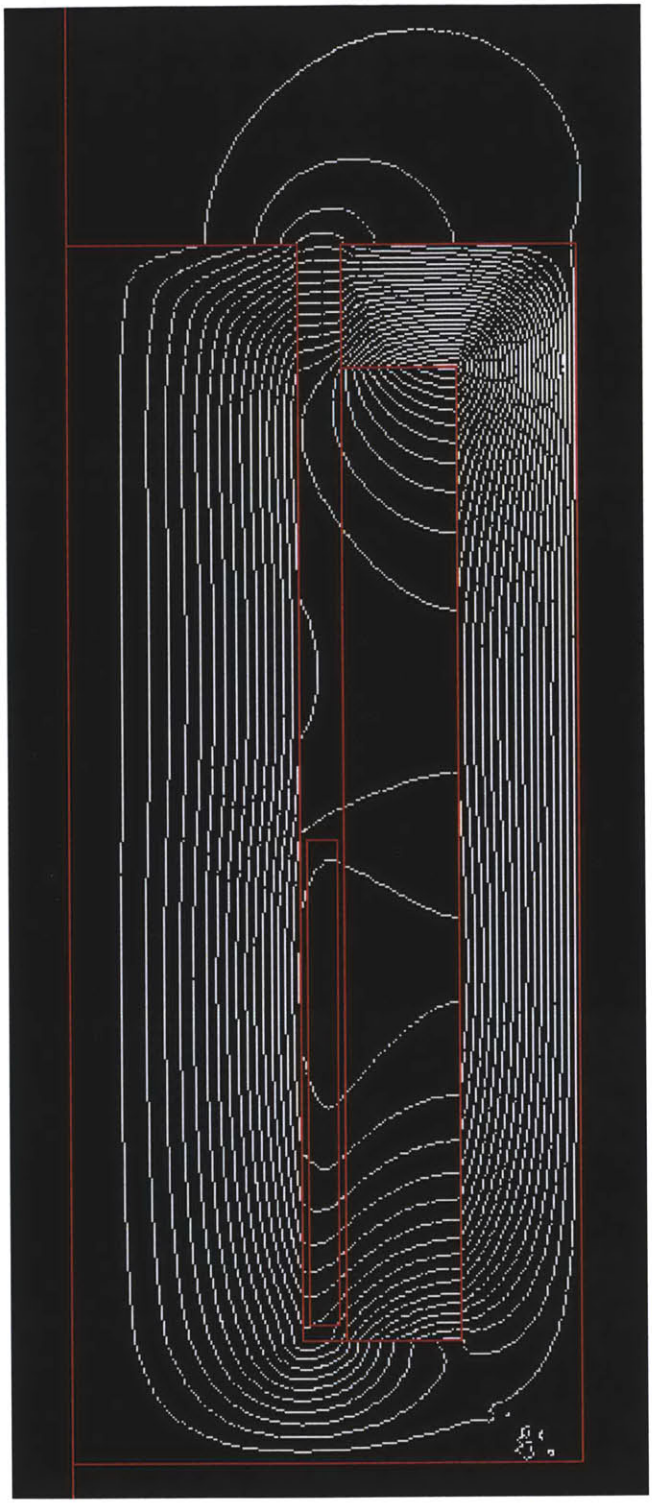

Figure 3-11: Magnetic flux lines with a current density of $3{\cdot}10^8$ A/m^2 at bottom stroke.

above the coil. The largest force output (622 N downwards) of the Lorentz-force model is produced when the coil is at the +15 mm offset and the current is flowing into the page. The magnetic loop is essentially one large loop identical to the previous scenario but in the opposite direction. However, the force does not decrease because there is no plate that provides a path for the magnetic loop to travel through. The magnetic flux still travels across the copper coil resulting in the high force output.

The material properties of the casing and magnet are crucial for performance and must be considered in the optimization of the Lorentz-force actuator. High permeability steel such as vanadium permendur can increase magnetic flux intensity at the tradeoff of being 100 times more expensive. Neodynium-Iron-Boron magnets come in various grades that are defined by their maximum energy product. Maximum energy product is defined by the magnetic field strength of the fully saturated magnetic material. The highest grade Neodynium-Iron-Boron magnet (N52) has a maximum operating temperature of 50°C [8]. It is assumed that the coil and magnet are the same temperature when obtaining an approximate upper bound for the operating temperature of the magnet. Consider the differential control volume $dxdydz$, an energy balance yields,

$$\rho c_p \frac{dT}{dt} dxdydz = I^2 R, \tag{3.3}$$

where ρ is the density of copper (8960 kg/m^3), c_p is the specific heat of copper (385 J/(kg·K), T is temperature (K), I is current (A), and R is resistance (Ω). Since,

$$I = J^2/A, \tag{3.4}$$

where J is current density (A/m^2) and,

$$R = \rho_{elec} \frac{l}{A}, \tag{3.5}$$

where ρ_{elec} is electrical resistivity (16.78 nΩ/m) [9], l is length (m), and A is cross

sectional area (m^2), then the conservation of energy reduces to,

$$\rho c_p \frac{dT}{dt} = \rho_{elec} J^2. \tag{3.6}$$

Assuming a maximum current density of $3 \cdot 10^8$ A/m^2 for a duration of 10 ms, the change in temperature of the coil is,

$$\Delta T = \frac{\rho_{elec} J^2}{\rho c_p} t = 4.39\ K, \tag{3.7}$$

which is well below the maximum operating temperature of N52 Neodynium-Iron-Boron if the coil's initial state is at room temperature. The low velocity phase of the heat generation is ignored because velocity is proportional to the current squared. Heat generation is then proportional to the fourth power of jet velocity.

Chapter 4

Rheological Properties

Because the Reynolds number of the water based injections were so high, the effects of viscosity could be ignored; consequently, the relationship between pressure and velocity was able to be determined from Bernoulli's principle. Assuming the jet velocity needs to be at least 150 m/s for a fluid with a viscosity of at least 1 Pa·s, the Reynolds number is calculated to be,

$$Re = \frac{\rho v d}{\mu} = 33. \tag{4.1}$$

Viscous effect will clearly dominate this flow profile. The total pressure required to drive a flow will arise from the flow through the orifice of the ampoule because the diameter is so small. The pressure drop along a circular pipe of length (L = 3 mm) and diameter (D = 221 μm) is,

$$\Delta P_{visc} = f \frac{L}{D} \frac{\rho v^2}{2} = 353 \text{ MPa}, \tag{4.2}$$

for a dimensionless friction factor of,

$$f = \frac{64}{Re} = 1.93. \tag{4.3}$$

For an ampoule with a cross sectional area of 10^{-5} m^2 the force required to achieve this pressure is at least 3530 N. This is a lower bound on the estimate because the

inertial effects of accelerating this flow from rest are ignored. There are two main challenges with generating a flow this large:

1. The old Lorentz-force actuator achieved pressures of up to 20 MPa.

2. The ampoule will fail at pressures this large.

The most significant contribution to the pressure drop is the diameter. Pressure drop is inversely proportional to the square of diameter. Increasing the orifice diameter to 500 μm corresponds to a Reynolds number of,

$$Re = \frac{\rho v d}{\mu} = 75. \tag{4.4}$$

For a friction factor of,

$$f = \frac{64}{Re} = 0.8533, \tag{4.5}$$

the new pressure required is calculated to be,

$$\Delta P_{visc} = f \frac{L}{D} \frac{\rho v^2}{2} = 69 \text{ MPa}. \tag{4.6}$$

This required pressure is a much more feasible value given the structural properties of an ampoule and the capabilities of smaller Lorentz-force actuators. Because the diameter of the orifice has increased, the piston must travel faster because the ratio of the area of the piston to the area of the orifice has decreased by conservation of mass. Transient inertial effects will become more significant as the diameter of the ampoule's orifice increases.

4.1 Fluid Characterization

Rheological measurements were performed on two samples of poly(ortho) ester and glycerin at various concentrations by volume. Viscosity and strain measurements were performed on the AR-G2 rheometer [10] in the Hatsopoulos Microfluids Laboratory.

Shear stress is defined as,

$$\tau_{xy} = \mu(\dot{\gamma})\frac{\partial v_x}{\partial y}, \tag{4.7}$$

where,

$$\dot{\gamma}_{ij} = \frac{\partial v_i}{\partial x_j}, \tag{4.8}$$

is the strain rate of the fluid. For Newtonian fluids, the magnitude of viscosity does not depend on $\dot{\gamma}$ and is therefore constant across all values of strain rate. A 2° cone with a diameter of 40 mm or 60 mm diameter spreads the fluid evenly throughout the gap and spins the fluid at a fixed strain rate. For an angular rotation of ω at an

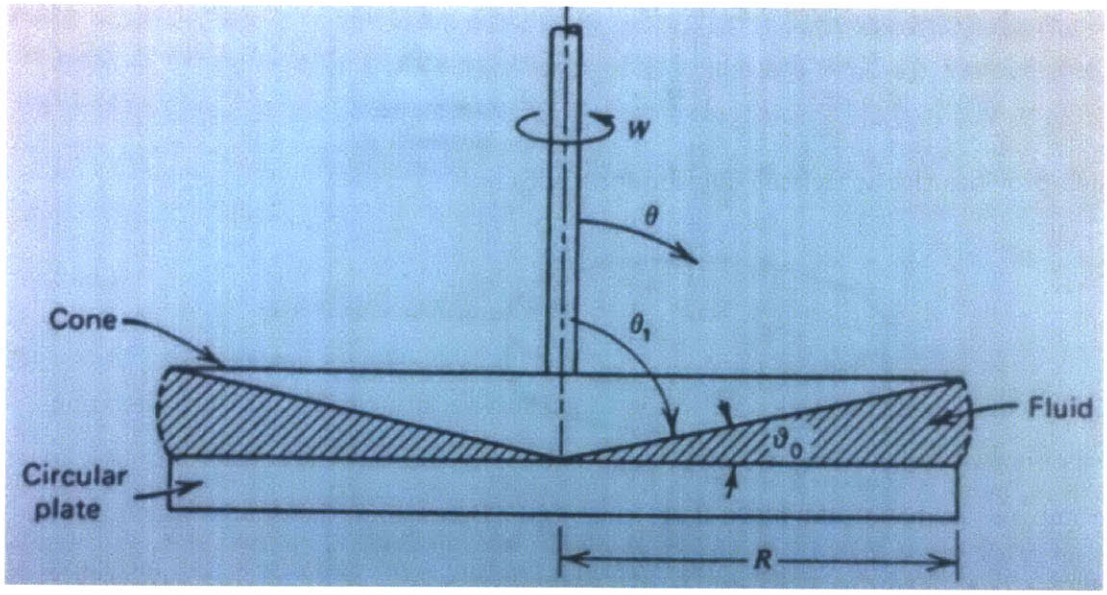

Figure 4-1: Depiction of a cone and plate couette flow taken from [11].

angle from the vertical defined by θ, the velocity in the angular direction at radius r for a cone with an angle θ_0 is defined as,

$$v_\phi(\theta) = \omega r\frac{(\pi/2) - \theta}{\theta_0}. \tag{4.9}$$

The shear rate is then,

$$\dot{\gamma}_{\theta\phi} = \frac{\sin(\theta)}{r}\frac{\partial}{\partial\theta}\left(\frac{v_\phi}{\sin(\theta)}\right) \approx \frac{1}{r}\frac{\partial}{\partial\theta}v_\phi = -\frac{\omega}{\theta_0}. \tag{4.10}$$

The approximation can be made since θ is about $\frac{\pi}{2}$, then the value of $\sin(\theta)$ is approximately unity within the flow. The torque acting on the flow is,

$$T = \int_0^{2\pi}\int_0^R \tau_{\theta\phi}|_{\theta=\frac{\pi}{2}} r^2 dr d\phi. \tag{4.11}$$

Looking at the velocity profile, it is easy to notice that the shear rate is constant throughout the gap, thus the shear stress is also constant throughout the gap. The shear stress is then,

$$\tau_{\theta\phi} = \frac{3T}{2\pi R^3}, \tag{4.12}$$

which provides the analytical solution for viscosity,

$$\mu = \frac{3T\theta_0}{2\pi R^3\omega}. \tag{4.13}$$

The consequence of this solution is that the viscosity can be measured for non-Newtonian viscosities because of the approximately constant shear rate throughout the gap of the cone and plate flow geometry. Because of the sparse amounts of poly(ortho) ester, the viscosity of glycerin at various concentrations was measured to see if it could be used as a substitute for testing with the needle-free injector. The flow procedure for the AR-G2 was ran in steady state flow step mode. This experimental flow maintains a steady shear rate for over a minute and then begins to measure torque. This process would then step up in shear rate, wait for the inertial effects to dissipate, and resume the torque averaging process. The AR-G2 is equipped with a Peltier device [12] to ensure the fluid is maintained at room temperature. The viscosity of glycerin was measured at shear rates from 10^{-3} s^{-1} to 10^3 s^{-1} with the 2°, 60 mm cone.

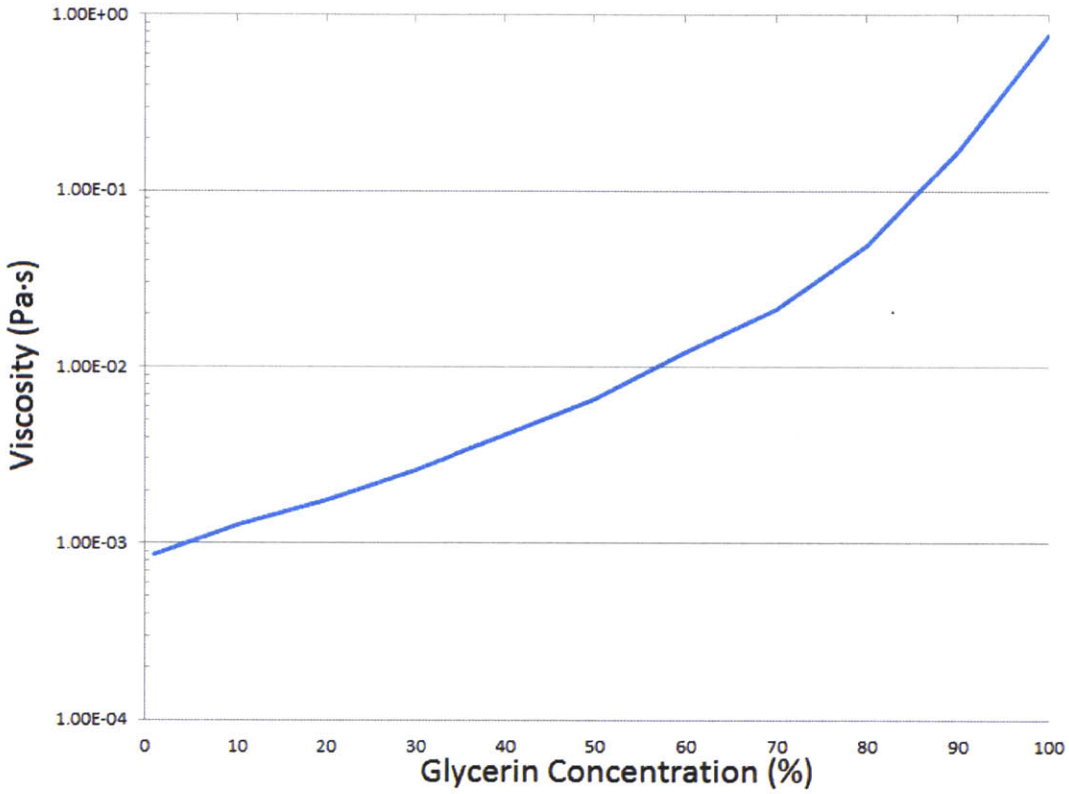

Figure 4-2: Viscosity of 50% concentration glycerin at various shear rates.

The large fluctuations at low shear rates are a result of insufficient resolution. Fluids of larger viscosity can be accurately measured at shear rates this low. Above a shear rate of about 0.1 s^{-2}, the AR-G2 is able to take sufficient measurements of the viscosity. There is a slight increase in the viscosity at high shear rates for the lower concentrations of glycerin. This arises from evaporation of water over the 30 minute duration of the flow experiment. The average viscosity within the operating envelope of the AR-G2 was used to find the relationship between viscosity and the concentration of glycerin.

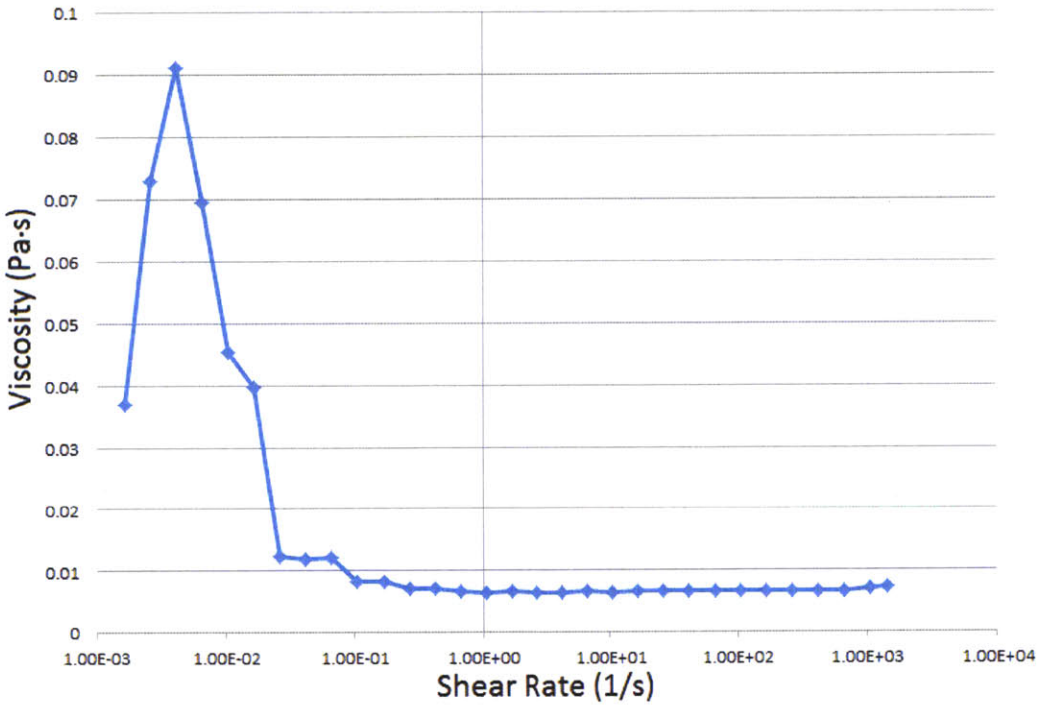

Figure 4-3: Viscosity as a function of glycerin concentration.

Because the flow within the ampoule is transient, the time-varying properties of a fluid cannot be ignored. The viscoelastic properties of certain polymeric fluids can be described by the Generalized Maxwell model. The dashpots represent the resistance to strain rate while the springs are energy storage elements that are dependent

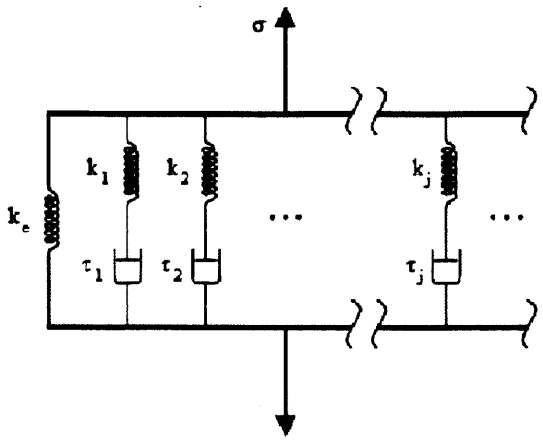

Figure 4-4: Generalized Maxwell Model taken from [13].

upon the magnitude of deformation. Each element of a spring and dashpot in series represents a relaxation time constant of the polymeric fluid. The properties of the fluid exhibit different properties upon pressurization based on the time scale of the flow. In order to characterize these properties, a small-amplitude oscillatory shear experiment was performed on the poly(ortho) ester samples. In order to determine the range of magnitudes of strain in which these properties were linearly viscoelastic, a strain sweep experiment was performed. The strain rate of small-amplitude oscillatory shear is described by,

$$\gamma_{yx}(0,t) = \gamma^0 \sin(\omega t), \tag{4.14}$$

and thus,

$$\dot{\gamma}_{yx}(t) = \gamma^0 \omega \cos(\omega t) = \dot{\gamma}^0 \cos(\omega t), \tag{4.15}$$

where γ^0 and $\dot{\gamma}^0$ are the shear strain and shear strain rate respectively. The shear stress will be of the form,

$$\tau_{yx} = -G'(\omega)\gamma^0 \sin(\omega t) - G''(\omega)\gamma^0 \cos(\omega t), \tag{4.16}$$

and,

$$\tau_{yx} = -\eta'(\omega)\dot{\gamma}^0 \cos(\omega t) - \eta''(\omega)\dot{\gamma}^0 \sin(\omega t), \tag{4.17}$$

which represents components of shear stress that are in phase and out of phase with the oscillatory strain and strain rate. For purely viscous fluids, G' is equal to zero. It can be seen that,

$$\eta' = \frac{G''}{\omega}. \tag{4.18}$$

Thus, the dynamic viscosity of a fluid is related to the loss modulus of oscillatory strain. The strain sweep experiment, for a given angular frequency, measures the values of G' and G'' at various values of strain.

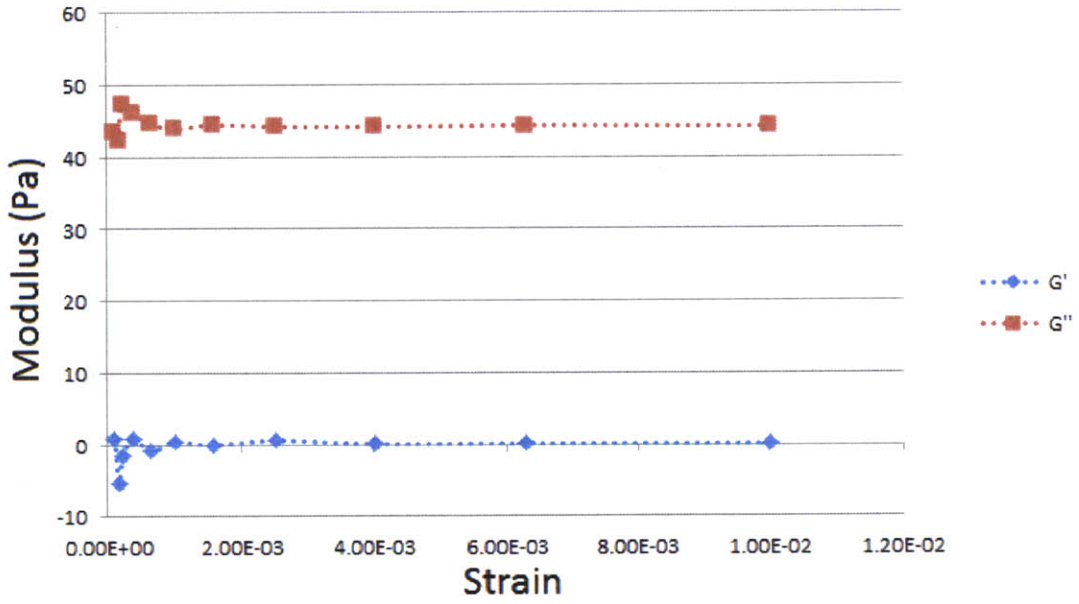

Figure 4-5: Values of G′ and G″ as a function of strain.

The values of G'' clearly dominate for the poly(ortho) ester sample. The non-zero values of G' at low strains are due to noise. These results exemplify the fact that this polymeric fluid is not elastic. The viscosity measurements of poly(ortho) ester were obtained using a 2° cone with a diameter of 60 mm. The increase in viscosity at the higher shear rates is due to the measured torque exceeding the operating envelope

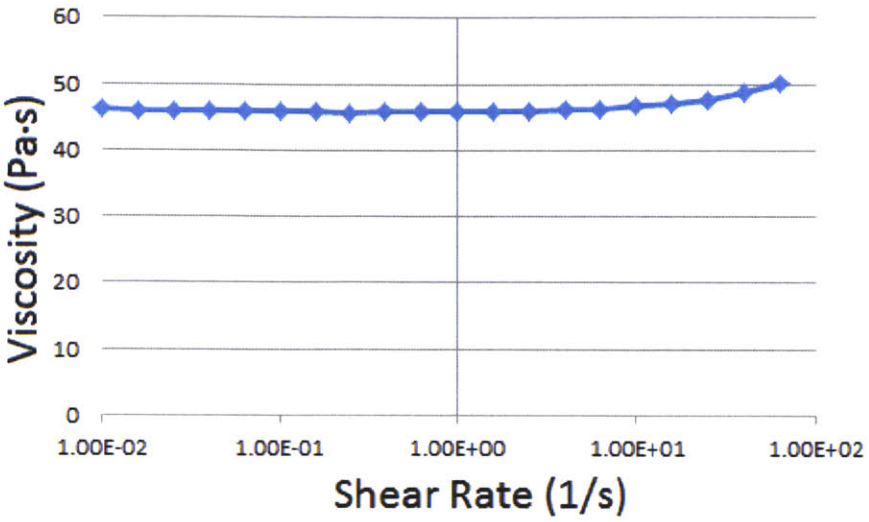

Figure 4-6: Viscosity of the first poly(ortho) ester sample as a function of shear rate.

of the AR-G2. These values were much higher than expected. Because the pressure required to drive a laminar flow at a given velocity is linearly proportional to viscosity, the pressure would have to be well over 1 GPa. Pressures this high exceed the ultimate tensile strength of most materials.

Another sample of poly(ortho) ester had a much lower viscosity. The viscosity of the new sample was measured with a 2° cone with a diameter of 40 mm. A smaller cone was chosen in order to reduce the required sample volume from 2 mL to 520 μL and to increase the operating shear rate of the AR-G2. The AR-G2 is ultimately limited to a maximum torque, thus smaller flow geometries provide larger maximum shear rates.

The viscosity of the new sample is even better than expected. Additionally, the poly(ortho) ester seems to be shear thinning at shear rates greater than 1000 s^{-1}. The effects of shear thinning are verified by the fact that none of the fluid was being ejected from the cone at high shear rates, furthermore, the measured torque continued to increase. Drastic reduction of measured viscosity due to fluid ejection would result in a decrease of measured torque, which would ultimately violate first principles. It

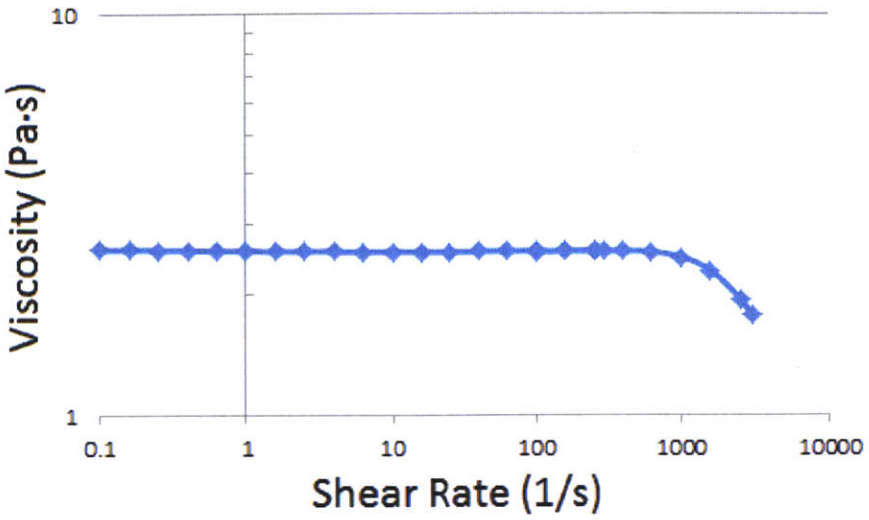

Figure 4-7: Viscosity of the second poly(ortho) ester sample as a function of shear rate.

is not possible to increase the velocity of a fluid by decreasing the torque. This non-Newtonian effect could not be observed in the first sample because the viscosity was too high to make measurements at shear rates of such magnitude. The cross model is used to describe the relationship between shear rate and the viscosity of shear thinning fluids. The viscosity is defined as,

$$\mu(\dot{\gamma}) = \frac{\mu_0}{1 + (\frac{\mu_0 \dot{\gamma}}{\tau})^{1-n}}, \tag{4.19}$$

where μ_0 is the zero shear rate viscosity, τ is the shear stress where the viscosity deviates from its constant value, and n is a coefficient describing how drastically the viscosity reduces at high shear rates. At low shear rates, the viscosity is essentially constant and the fluid behaves like a Newtonian fluid. At large shear rates, the fluid behaves like a power-law fluid. The viscosity measurements were fit to a cross-fluid model with the parameters of $\mu_0 = 2.6$ Pa·s, $\tau = 4000$ Pa, and $n = -1$.

The shear thinning properties of poly(ortho) ester has significant effects for the shear rates at jetting velocities. The shear rate of a flow in a circular pipe is largest

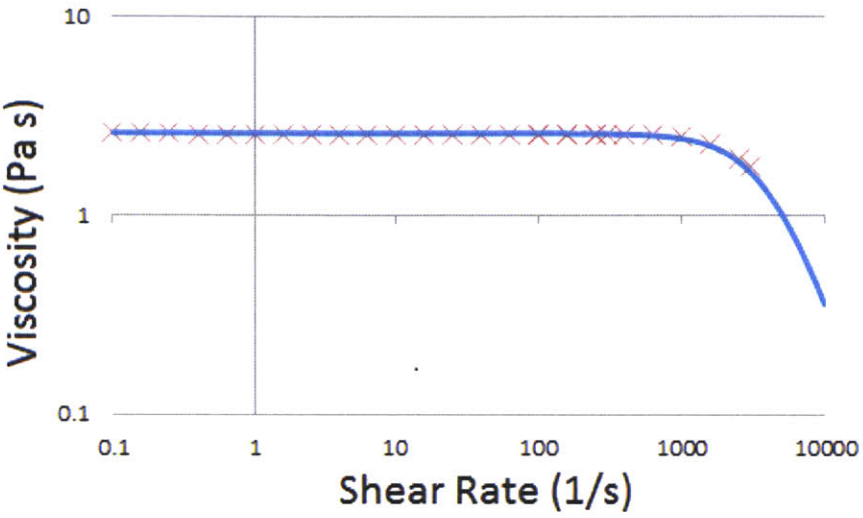

Figure 4-8: The cross fluid model fitted to the second poly(ortho) ester batch.

at the walls. Recall that ΔP_{visc} is the pressure drop due to viscous effects of a flow in a pipe, a pressure balance therefore yields,

$$\Delta P_{visc}\pi\frac{D^2}{4} = \tau_w \pi D L. \tag{4.20}$$

The shear stress at the wall is calculated to be,

$$\tau_w = \frac{\Delta P_{visc} D}{4L} = 6.5 \text{ MPa}, \tag{4.21}$$

for the initially calculated ΔP_{visc} of 353 MPa. Assuming the viscosity is constant, the shear rate at the wall will be at least,

$$\dot{\gamma} = \frac{\tau_{yx}}{\mu} = 2.5 \cdot 10^6 \ s^{-1}, \tag{4.22}$$

for a fluid with a constant viscosity of 2.5 Pa·s. Since the shear rate in the fluid at the wall is orders of magnitude above the maximum shear rate measured by the rheometer, the viscosity could continue to reduce in value. Shear-thinning has the

potential to significantly reduce the pressure required to achieve jet velocities of at least 150 m/s.

Chapter 5

Lorentz-Force Actuator Characterization

For the purposes of driving more viscous drug mediums with the needle-free injector, a Lorentz-force actuator must be powerful enough to deliver high forces over very short periods of time. Based on the calculations for the pressure required in the previous chapter, the maximum force output should be at least 1000 N, but preferably over 2000 N for 10 ms. The Lorentz-force actuator chosen for this application was the BEI Kimco LA25-42-000A [14]. In order to determine the maximum possible output of this actuator, two design challenges of the experimental setup had to be considered:

1. The power supply has to deliver incredibly high power (>10kW) over a short period of time.

2. The force measuring instrument needs to have very high bandwidth.

5.1 Providing the Power

The output of the Lorentz-force actuator is ultimately limited to the temperature of the coil. The design is limited to the specification of a maximum operating temperature of 155°C provided by the manufacturer. Although the specifications of the LA25-42-000A state that the maximum peak force is 267 N, this value is sustained

for only 10 seconds. Since the time scale of an injection is many orders of magnitude below this duration, the max force output can be much higher. The continuous stall force of the actuator is $F_n = 86.3$ N. Since the actuator is stalled, all of the energy being input into the system will be dissipated as heat. Because the actuator constant $A_c = 13.79\ \mathrm{N}/\sqrt{W}$, the power consumption,

$$\dot{Q} = \left(\frac{F_{stall}}{A_c}\right)^2 = 39\ W, \tag{5.1}$$

is also the amount of heat dissipated by the Lorentz-force actuator at a steady state temperature of 155°C. In order to have an upper bound estimate of the instantaneous heat generation that the coil can handle, power consumption of the actuator at peak force must be considered. The resistance of the coil is $R_c = 2.4\ \Omega$ and the current at peak force output is $I_p = 12.5$ A. The heat generated by the coil is,

$$\dot{Q} = I_p^2 R = 375\ W. \tag{5.2}$$

For the sake of not approaching the maximum heat generation, it is assumed that the coil is dissipating heat through convection at the maximum rate of 39 W for the entire 10 second duration. The energy change in the coil at maximum load for 10 seconds is then,

$$\Delta E = (I_p^2 R - (\frac{F_{stall}}{A_c})^2)t = 3360\ J. \tag{5.3}$$

A safety factor of at least 2 was established in order to prevent permanent damage to the Lorentz-force actuator. When choosing a power supply to drive this coil, an upper bound estimate on the energy provided will assume that no heat transfer to the ambient occurs. Capacitors are known for their high power densities; consequently, a 5400 μF, 500 V Cornell Dublier Electronics capacitor (550C542T500DN2B) [15] was chosen to provide the high current needed for significant force output. The total energy stored by the capacitor is,

$$E = \frac{1}{2}CV^2 = 675J, \tag{5.4}$$

which is well below the maximum instantaneous energy change that the coil can handle assuming lossless energy transfer from the capacitor to heat dissipated in the coil. The physics describing the discharging of the capacitor across the Lorentz-force actuator can be modeled by a simple RLC circuit connected in series. The differential equation describing this undriven system is,

$$L\frac{\partial^2 I(t)}{\partial t^2} + R\frac{\partial I(t)}{\partial t} + \frac{1}{C}I(t) = 0, \tag{5.5}$$

for an inductance $L = 2.5$ mH, $R = 2.421\ \Omega$, and $C = 5400\ \mu$F. The characteristic roots of this differential equation are,

$$m_{1,2} = -\frac{R}{2L} \pm \frac{1}{2}\sqrt{\frac{R^2}{L^2} - \frac{4}{LC}} = -84.6;\ -875.4. \tag{5.6}$$

The general solution is then,

$$I(t) = Ae^{m_1 t} + Be^{m_2 t}. \tag{5.7}$$

While the first initial condition is clearly,

$$I(0) = 0, \tag{5.8}$$

the second condition arises from the initial current of 0 A. Since there is no current flowing through the circuit, the intial voltage V_0 stored in the capacitor is completely opposed by the voltage stored in the inductor. Since,

$$L\frac{dI}{dt} = V_0, \tag{5.9}$$

the initial conditions can be used to solve for the constants of integration,

$$A = -B = \frac{V_0}{L(m_1 - m_2)} = 252.9. \tag{5.10}$$

Since the constant of integration is linearly proportional to the initial voltage of the capacitor, the maximum current achieved in this system is also linearly proportional to the initial voltage. At 500 V, the current reaches 178 A at a time of 3 ms which is

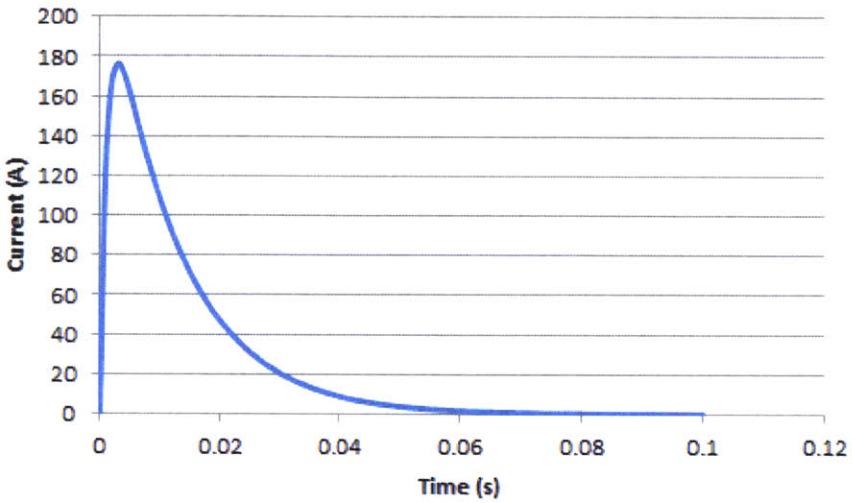

Figure 5-1: Current through RLC circuit with an initial voltage of 500 V.

almost 15 times the current at 10 seconds of peak force. Because the current density is so high, for the reasons described in the electromagnetic modeling chapter, the relation between force and current will deviate from linearity. The solution of the differential equation is verified by taking the integral,

$$\int_0^\infty (I(t))^2 R dt = 675\ J, \tag{5.11}$$

which demonstrates that the energy stored in the capacitor is equal to the energy dissipated by the resistor.

5.1.1 Charging the Capacitor

A Hewlett Packard 500 V DC power supply (6035A) was used to charge the capacitor. A Cynergy 3 reed relay (DAR70510) [16] was used as protection against current due to

the capacitor discharge. The coil of the relay was powered by a Hewlett Packard DC power supply (E3610A) at 5 V and was toggled by a mechanical switch. The general approach was to connect the capacitor to the supply, switch the relay, and slowly increase the voltage up to 500 V. Because the internal resistance of the capacitor is 26.1 mΩ, small differences in voltage between the power supply and the capacitor will greatly exceed the current limit of the power supply. A power resistor was connected in series between the capacitor and power supply in order to reduce the current of the system while an 800 V, 2 A rated diode manufactured by Micro Commercial Co. (RL206-TP) [17] provided circuit protection in case the voltage of the power supply happened to drop to zero. A power resistor with a resistance of 50 Ω and a dissipation rating of 100 W was chosen. To keep the current to a safe level of 1 A, the voltage difference between the power supply and the capacitor must never exceed 50 V. Since,

$$\frac{V}{R} = I = 1\ A, \tag{5.12}$$

the power dissipated by the resistor is,

$$P = I^2 R = 50\ W, \tag{5.13}$$

which is half of the maximum allowable value. The time constant to charge the capacitor is,

$$\tau = RC = 0.27\ s. \tag{5.14}$$

If the power supply was instantaneously turned to 50 V, it took about 1 second for the capacitor to reach 50 V. Because the time constant was so small, it was possible to slowly, but continuously increase the voltage of the power supply to 500 V. It was important to pay attention to the power supply to make sure the current did not exceed 1 A.

5.1.2 Discharging the Capacitor

The discharging of the capacitor was controlled by a silicon controlled rectifier (SCR). The SCR manufactured by Littelfuse (S8065KTP) [18] is rated for 800 V and a non-repetitive peak current surge of 800 A for a half sine wave at 50 Hz. Because the approximate period of the 178 A peak is about twice as long, a current rating of 800 A was chosen to provide a safety factor of over 2. An SCR is in its normal off state until its gate voltage exceeds a certain threshold. The gate voltage was supplied by the HP 5 V supply and was toggled by a push button. When the SCR turns on, it will stay in the on state until there is no more current flowing through. Although this does not provide good switching rates, it is appropriate for discharging a capacitor.

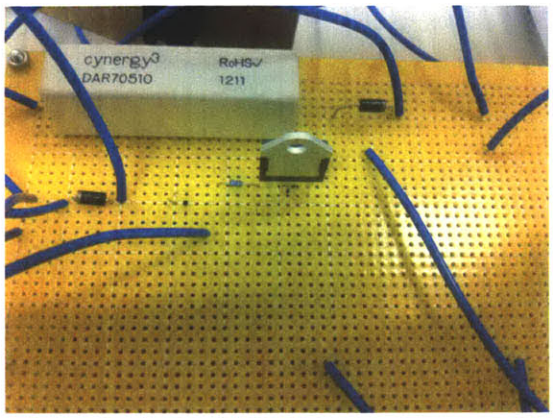

Figure 5-2: Printed circuit board that drives the Lorentz-force actuator.

5.2 The Benchtop Device

The BEI Kimco LA25-42-000A must be mounted to a frame that can support the force output of the actuator. The top mounting plate of the frame is a 160 mm × 160 mm × 12.7 mm aluminum plate that was milled to allow M8 clearance holes and counter bores that mate to the frame. The inner clearance holes and counter bores were milled for 6-32 bolts that couple to the base of the Lorentz-force actuator. A

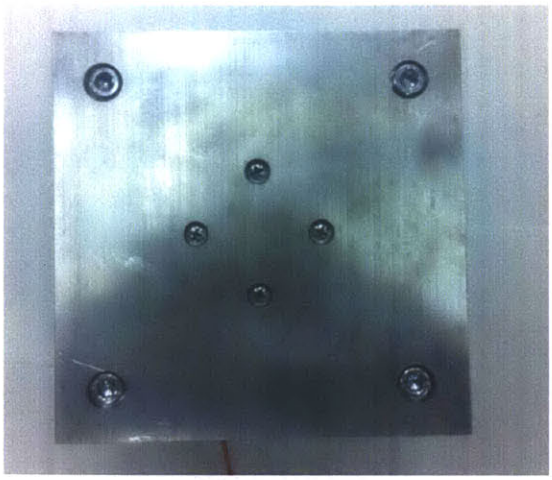

Figure 5-3: Top mounting plate.

160 mm × 160 mm × 16.1 mm aluminum plate was machined with identically placed M8 clearance holes and counter bores to serve as the bottom mounting plate for the frame of the benchtop device.

Because the onset of peak force is under 10 ms, normal s-shaped load cells do not have the sufficient bandwidth for this particular application. A piezo-based loadcell (Omega DLC101-500) [19] with a bandwidth of 25 kHz and a maximum force rating of 2224 N was chosen. Because of the capacitive nature of piezoelectric-based force measurements, this particular load cell is not suitable for static load measurements. A mounting plate was machined to couple the coil of the Lorentz-force actuator to the load cell. The 64 mm × 64 mm × 10.1 mm aluminum plate had clearance holes and counter bores milled for four 10-32 bolts that mate the plate to the coil. A central clearance hole and counter bore for a 1/4-28 bolt was machined on the other side of the plate to couple to the load cell. Four 3.2 mm holes were drilled to line up with the exhaust holes of the coil in order to reduce pressure-induced drag when the coil moves inwards.

The frame was made using MK 40 Series aluminum framing profiles. Two sets of two 40 series profiles were cut with a cold saw to a length of 160 mm to mate

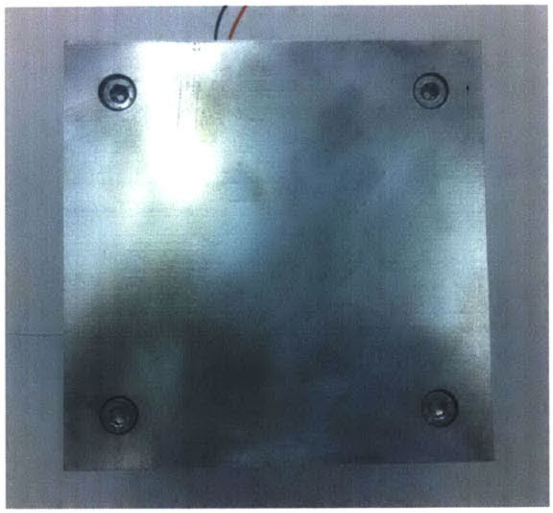

Figure 5-4: Bottom mounting plate.

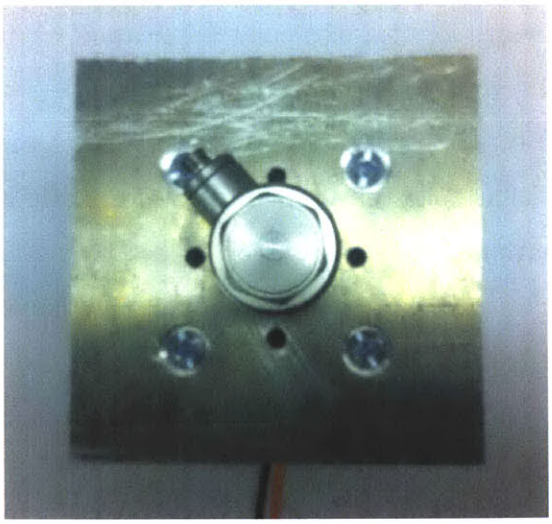

Figure 5-5: Coupling plate betwen the coil and the load cell.

to the top and bottom mounting plates. The height of the frame was determined by measuring the total height of the actuator, coupling plate, and load cell when assembled together. The height needed to be sufficient to allow the coil to be slightly beyond mid stroke when the load cell was in contact with the bottom mounting plate. Shims could then be incorporated to make measurements of force output at various stroke lengths. Four MK 40 series profiles were cut with a cold saw to a length of 57 mm. In order for the 57 mm legs to support the tension generated by the Lorentz-force actuator, tension plugs were required to couple the legs to the 160 mm supports. 10 mm through holes were drilled at a distance of 15 mm from each end to allow the M8 set screws to fasten to the tension plugs.

5.3 Results and Discussion

A National Instruments data acquisition unit (USB-6215) [20] acquired the raw data from the load cell at a sampling rate of 50 kS/s and outputted it to a viewable form through a LabView virtual interface [21]. The sensitivity of the piezoelectric load cell is 2.2 mV/N after being amplified by an Omega accelerometer power supply (ACCPS3A) [22]. After closing the relay, the voltage was incrementally increased just beyond the desired voltage due to the discharging effects of the bleed resistor. Once the Fluke multimeter (True RMS 187) displayed the desired capacitor voltage, the silicon controlled rectifier was triggered to discharge the capacitor.

The time to peak of the Lorentz-force was about 4 ms for the voltages above 150 V and 5 ms for the voltages below 50 V. The ringing of the system had an approximate frequency of 715 Hz. The ringing is due to second order effects arising from the mechanical admittance of the frame supporting the Lorentz-force actuator. Measurements with negative force values were also observed, but this was attributed to the time constant of the capacitor-like effect of the piezoelectric load cell reaching a steady state value of zero. The relationship between initial voltage and the measured peak force provides insight into the behavior of this system.

The peak force value provided in the specifications of the LA25-41-000A was

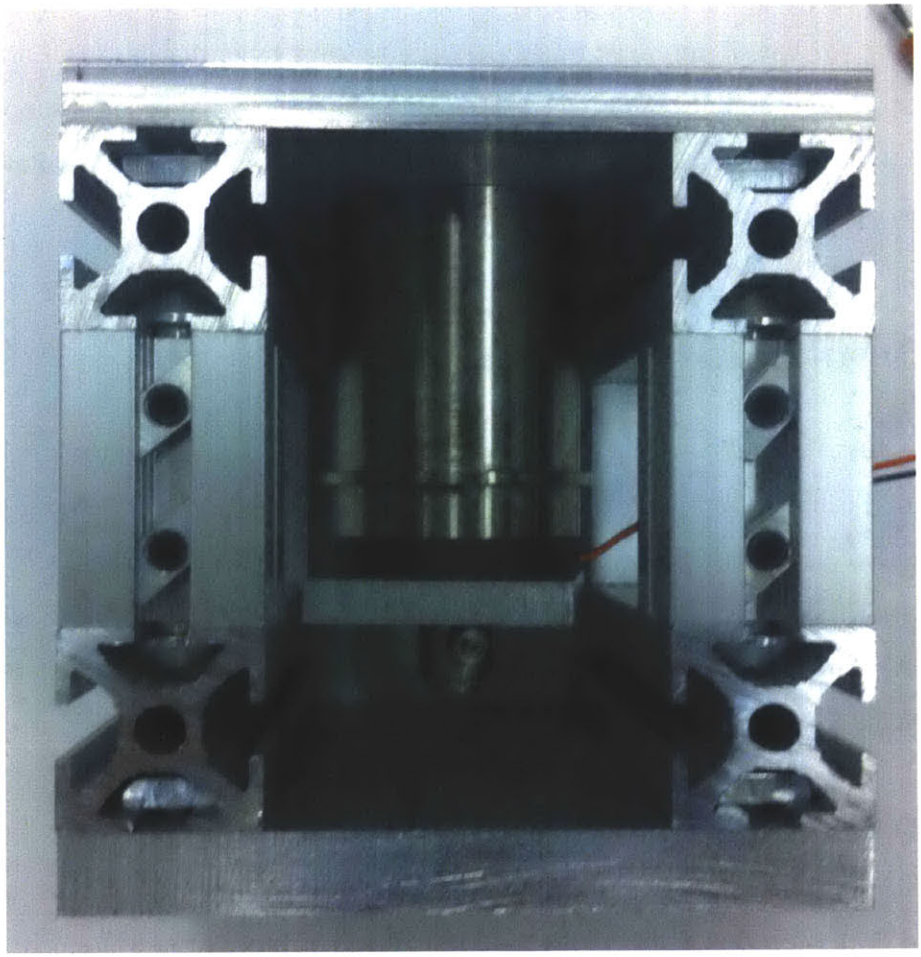

Figure 5-6: Full frame supporting the Lorentz-force actuator and load cell.

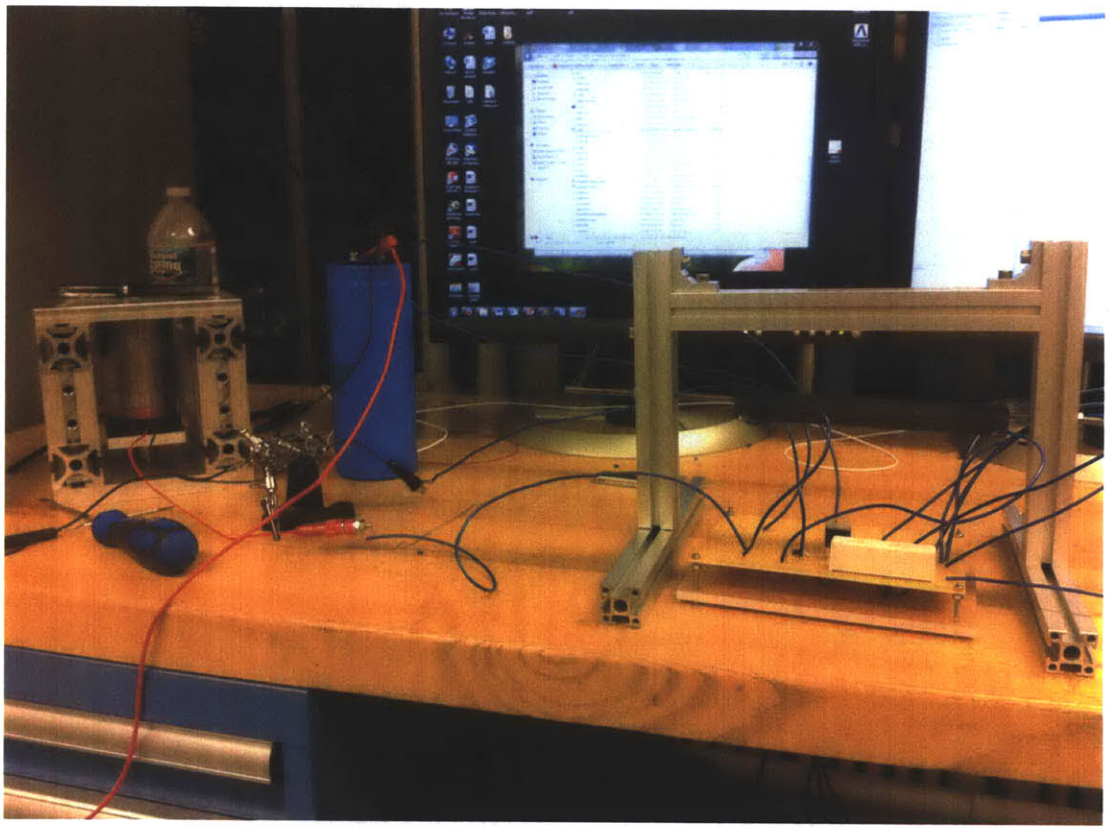

Figure 5-7: Benchtop experiment showing the circuit conected to the capacitor and Lorentz-force actuator.

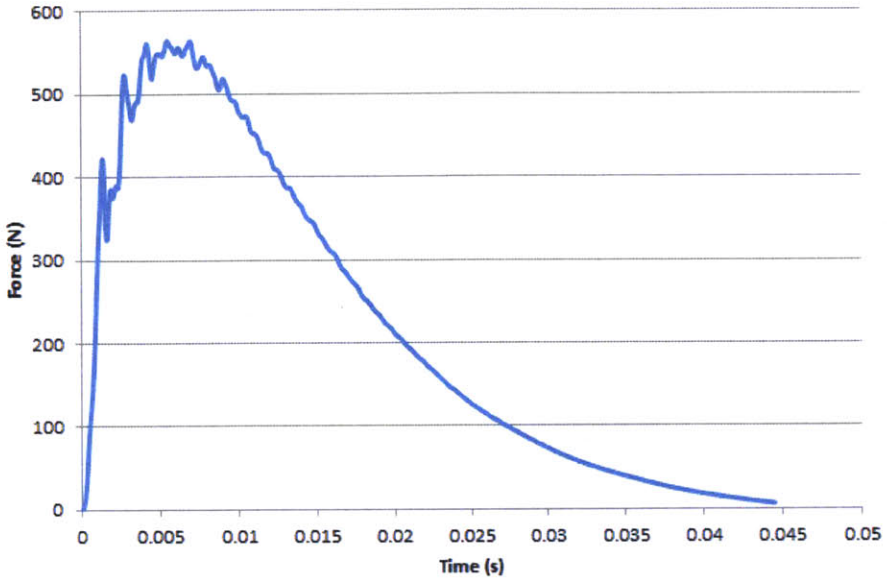

Figure 5-8: Measured Lorentz-force for an initial voltage of 100 V.

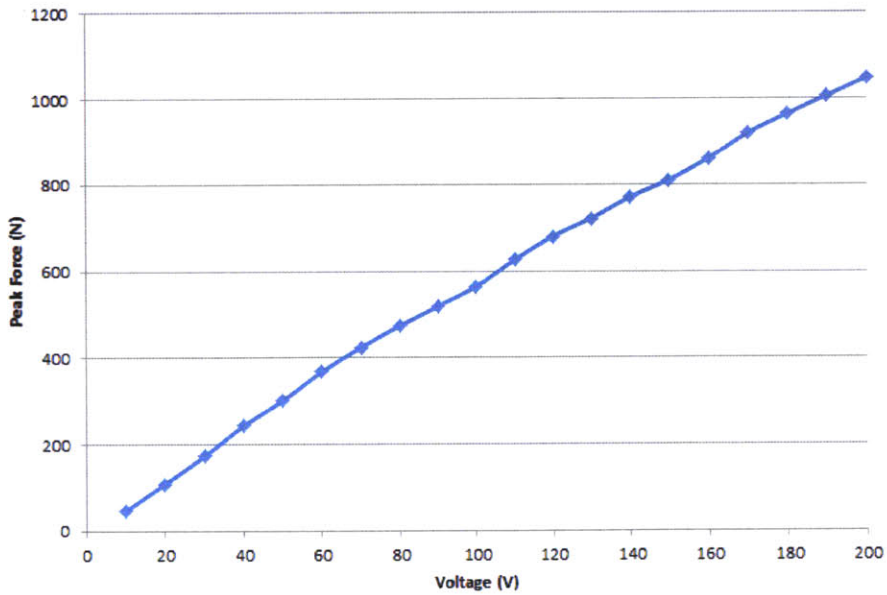

Figure 5-9: Measured peak Lorentz-force for various initial capacitor voltages.

exceeded at a capacitor voltage of just over 40 V. The DC voltage required to achieve a force this large was 30 V. The difference between these two voltages was caused by the damping from the resistance in the second order system. Although the relationship between peak force and voltage seems to be approximately linear, a fitted linear function will not account for saturation at higher values of current.

Inefficiencies ultimately arise in this system because it is not simply an RLC circuit. Contact resistance, switching speeds, and saturation in the iron will result in a relationship between peak force and voltage that is not ideal. To adequately quantify the aforementioned inefficiencies, the peak force for a given voltage should be compared to the ideal peak force of the Lorentz-force actuator. The ideal peak force of the Lorentz-force actuator is defined as,

$$F_{ideal} = I_{ideal} B_c, \tag{5.15}$$

where $B_c = 21.35$ N/A is the actuator constant and I_{ideal} is the peak current of the ideal RLC circuit for a given initial capacitor voltage. The efficiency,

$$Q = \frac{F_{meas}}{F_{ideal}}, \tag{5.16}$$

was calculated for all initial capacitor voltages. An efficiency value significantly below 1 across all voltage values means that the current in the system never reached the ideal levels of the RLC circuit. This is due to the additional damping from increased contact resistance. The increasing behavior of efficiency at low voltages stems from the anode to cathode voltage being close to the gate to cathode voltage of the silicon controlled rectifier. The switching efficiency asymptotically approaches its maximum at around 40 V. The regime of constant efficiency demonstrates a linear relationship between peak force and applied voltage. The tapering decrease at 70 V and beyond signifies the onset of saturation within the steel of the Lorentz-force actuator. Beyond this voltage, there will be diminishing returns from increasing the capacitor voltage. As the initial voltage increases, the effects of saturation will become more prominent.

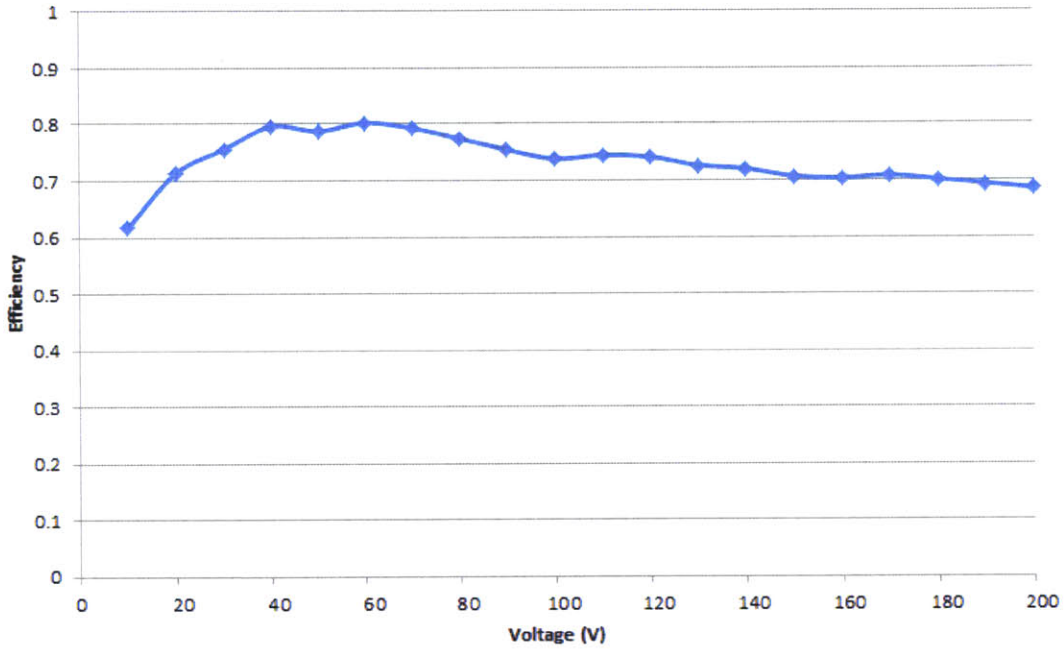

Figure 5-10: Measured efficiency for various initial capacitor voltages.

Chapter 6

Conclusion

A new Lorentz-force actuator magnetic configuration was designed and modeled using finite element modeling software. The magnetic solution was solved and used to calculate the approximate force acting on the coil. The radially-magnetized ring configuration generated a maximum pushing force of about 600 N, which corresponds to a pressure of 60 MPa in the current ampoule. Although the design is intended for liquids having a viscosity of about 10^{-3} Pa·s, more viscous injection mediums will require a much larger actuator. Poly(ortho) ester has been considered a potential medium for needle-free injections; consequently, its rheological properties were measured on the AR-G2 rheometer in the MIT Hatsopoulos Microfluids Laboratory. A viscosity model was fitted to the measured data to account for the shear thinning at high shear rates. For future viscosity measurements, the shear rate should be taken as high as possible in order to measure the extent to which poly(ortho) ester shear thins. Although the viscosity will asymptotically approach an infinite shear rate value, it will be useful to know how much smaller it is in comparison to its zero shear rate viscosity.

The force output of a BEI Kimco Lorentz-force actuator was measured to see if it had the appropriate strength to inject highly viscous fluids. The benchtop experiment designed to make these measurements consisted of the Lorentz-force actuator and its supporting frame, a capacitor to discharge across the actuator, and a circuit that operates the charging and discharging of the capacitor. For reasons including safety

and the preservation of the circuit, the stored voltage in the capacitor was limited to 200 V. For future research, a project box will be made to store the electrical components to prevent damaged caused by a failed capacitor. The circuit will also need to be redesigned for higher current ratings and lower resistances across the circuit with the hopes of maximizing the force output at 500 V.

Bibliography

[1] Hemond, B.D., Wedell, D.M., Hogan, C., Taberner, A.J., and Hunter, I.W., "A Lorentz-Force Actuated Autoloading Needle-free Injector," *Proceedings of the 28th Annual International Conference of the IEEE EMBS*, August 2006.

[2] Taberner, A.J., Ball, N.B., Hogan, C., and Hunter, I.W., "A Portable Needle-free Jet Injector Based on a Custom High Power-density Voice-coil Actuator," *Proceedings of the 28th Annual International Conference of the IEEE EMBS*, August 2006.

[3] Stachowiak, J.C., Muhlen, M.G., Li, T.H., Jalilian, J., Parekh, S.H., and Fletcher, D.A., "Piezoelectric Control of Needle-free Transdermal Drug Delivery," *Journal of Controlled Release*, Vol. 1, 124, pp. 88-97, August 2007.

[4] Heller, J., Barr, J., Ng, S.Y., Abdellauoi, K.S., and Gurny, R., "Poly(ortho esters): Synthesis, Characterization, Properties, and Uses," *Advance Drug Delivery Reviews*, Vol. 1, 54, pp. 1015-1039, June 2002.

[5] Taberner, A.J., Hogan, C., and Hunter, I.W., "Real-time Feedback-controlled Needle-free Jet Injection Using Linear Lorentz-force Motors," *Journal of Controlled Release*, Unpublished, 2010.

[6] Wendell, D.M., Hemond, B.D., Hogan, N.C., Taberner, A.J., and Hunter, I.W., "The Effect of Jet Parameters on Jet Injection," *Proceedings of the 28th Annual International Conference of the IEEE EMBS*, August 2006.

[7] ANSYS, "Electromagnetics Solutions,"
www.ansys.com/Products/Simulation+Technology/Electromagnetics.

[8] Dexter Magnetic Technologies, "N5211," www.dextermag.com/N5211.

[9] Copper Info, "Copper Properies,"
www.copperinfo.com/aboutcopper/properties.html.

[10] TA Instruments, "AR-G2 Rheometer,"
www.tainstruments.com/product.aspx?siteid=11&id=43&n=1.

[11] Bird, R.B., Armstrong, R.C., Hassager, O., *Dynamics of Polymeric Liquids*, 2nd Edition, John Wiley & Sons, New York, 1987.

[12] TA Instruments, "AR Rheometer Temperature Systems and Accessories," www.tainstruments.com/pdf/ARAccessorybrochure2009.pdf.

[13] Wikipedia, "Generalized Maxwell Model," www.en.wikipedia.org/wiki/GeneralizedMaxwellmodel.

[14] BEI Kimco, "LA25-42-000A," www.beikimco.com/pdf/LA25-42-000A.pdf.

[15] Cornell Dubler Electronics, "Type 550C," www.cde.com/catalogs/550C.pdf.

[16] Digikey, "D-Series High Voltage Reed Relays," www.media.digikey.com/pdf/DataSheets/Cynergy3PDFs/DSeries.pdf.

[17] Mirco Commercial Components, "RL201 through RL207," www.61.222.192.61/mccsemi/up_pdf/RL201-RL207(DO-15).pdf.

[18] Littelfuse, "65 / 70 Amp Standard SCRs," www.littelfuse.com/data/en/Data_Sheets/Littelfuse_Thyristor_Sxx65x_Sxx70x.pdf.

[19] Omega, "DLC101 Series," www.omega.com/Pressure/pdf/DLC101.pdf.

[20] National Instruments, "DAQ M Series," www.ni.com/pdf/manuals/371931f.pdf.

[21] National Instruments, "LabView," www.ni.com/labview.

[22] Omega, "ACC-PS Series," www.omega.com/Pressure/pdf/ACC-PS3A_ACC-PS4A.pdf.